IMPROVED ICE ACCRETION PREDICTION TECHNIQUES BASED ON EXPERIMENTAL OBSERVATIONS OF SURFACE ROUGHNESS EFFECTS ON HEAT TRANSFER

by

KEIKO YAMAGUCHI

S.B., Massachusetts Institute of Technology
(1988)

Submitted in Partial Fulfillment of
the Requirements for the Degree of

Master of Science
in
Aeronautics and Astronautics

at the

Massachusetts Institute of Technology
May 1990

Signature of Author_____
Department of Aeronautics and Astronautics
May 1990

Certified by_____
Associate Professor R. John Hansman
Department of Aeronautics and Astronautics
Thesis Supervisor

Accepted by_____
Professor Harold Y. Wachman
Chairman, Department Graduate Committee

Improved Ice Accretion Prediction Techniques Based on Experimental Observations of Surface Roughness Effects on Heat Transfer

by

Keiko Yamaguchi

Submitted to the Department of Aeronautics and Astronautics
in partial fulfillment of the requirements for the
Degree of Master of Science

Abstract

The use of surface roughness in the LEWICE ice accretion prediction code is examined. It was found that roughness is used in two ways: to determine the laminar to turbulent transition location and to calculate the turbulent heat transfer coefficient. The heat transfer coefficient computed by the LEWICE code was compared to a set of known experimental results, and the effects of surface roughness, boundary layer transition, and viscous flow field were analyzed. A series of experimental investigations focused on the study of the cause and effect of roughness on accreting glaze ice surfaces were conducted. Distinct zones of surface water behavior were observed, and the effects of icing cloud parameters on the transition from smooth to rough zones were studied. The location of the transition was found to migrate towards the stagnation with time, and its behavior appeared to be controlled by boundary layer transition and bead formation mechanisms at the interface between the smooth and rough zones. A simple multi-zone modification to the current ice accretion model was proposed based on the experimental observations. A preliminary version of this model was implemented in the LEWICE ice accretion prediction code, and compared with experimental ice shapes. For the cases run, the multi-zone model significantly improved the prediction of the glaze ice shapes.

Thesis Supervisor: Dr. Robert John Hansman
Associate Professor of Aeronautics and Astronautics

Acknowledgements

I would like to thank all those who have helped me over the last two years. First, Professor John Hansman, for all his advice and encouragement while working on the icing project. Dr. Jim Riley of the FAA Technical Center, for valuable information concerning LEWICE and taking time to answer all the questions I had. BF Goodrich De-Icing Systems, for the use of the icing wind tunnel facilities. NASA Lewis Research Center, especially Mark Potapczuk, for the use of the Icing Research Tunnel and his advice. Finally, the undergraduates who have helped me over the past two years, preparing for the experiments and running LEWICE on the computer.

Special thanks goes to my officemates in 37-450, for their patience, especially Craig, Vic, and Andy. I would also like to thank my family for their support, and Pierre, for just being there, always.

This project was supported in part by the National Aeronautics and Space Administration and the Federal Aviation Administration under Grants NAG-3-666 and NGL-22-009-640.

Table of Contents

List of Figures

List of Tables

Nomenclature

c_f	skin friction coefficient
C_p	specific heat of air, [J/kg°K]
h	heat transfer coefficient, [W/m^2°K]
h_l	laminar heat transfer coefficient, [W/m^2°K]
h_t	turbulent heat transfer coefficient, [W/m^2°K]
k	thermal conductivity, [W/m°K]
k_o	reference thermal conductivity, [W/m°K]
k_l	laminar roughness element height, [m]
k_s	equivalent sand grain roughness, [m]
k_t	turbulent roughness element height, [m]
LWC	liquid water content, [g/m^3]
MVD	mean volumetric diameter, [microns]
Nu	Nussult number
Pr	Prandtl number
Pr_t	turbulent Prandtl number
Re	Reynolds number based on freestream velocity
Re_l	local Reynolds number based on roughness element
s	distance along the surface from stagnation point, [m]
St	Stanton number
St_k	roughness Stanton number
s_{tr}	distance along the surface from stagnation point to the boundary layer transition point, [m]
T	temperature, [°C, °F, °R, °K]
T_o	reference temperature, [°C]
u_e	surface velocity, [m/s]

u_k	velocity at distance k from the surface, [m/s]
u_τ	shear velocity, [m/s]
V	freestream velocity, [m/s]
β	collection efficiency
δ	boundary layer thickness, [m]
λ	thermal conductivity of air, [W/m°K]
μ	dynamic viscosity, [kg/ms]
ν	kinematic viscosity, [m^2/s]
θ_l	laminar momentum thickness, [m]
θ_t	turbulent momentum thickness, [m]
ρ	density of air, [kg/m^3]

1. Introduction

1.1. Background

Ice will form on the exposed surfaces of an aircraft, such as the leading edge, the control surfaces, or the engine inlets, when it encounters an icing cloud, consisting of supercooled water droplets or freezing rain. Operation of an aircraft in icing conditions can be dangerous due to performance degradation, and often requires the detection and removal or prevention of ice formation.

The need for aircraft to be certified and to operate in all weather conditions has led to requirements for testing of aircraft to be certified for flight in icing conditions. Flight testing in natural icing conditions is not only expensive and time consuming, but also potentially dangerous, placing considerable emphasis on testing in icing wind tunnels. However, icing tests have operational limitations which decrease the range of icing conditions that can be evaluated. Hence there is a need for the accurate numerical prediction of ice accretion for any icing condition, given the shape and velocity of the accreting body.

The shape of accreted ice depends on several parameters which define the icing cloud: the total amount of water in the cloud, the liquid water content (LWC); the distribution of droplet sizes which is often characterized by the Median Volumetric Diameter (MVD); and the freestream temperature. The shape also depends on the geometry of the accreting body and its velocity. Icing clouds usually occur at altitudes below 22,000 ft, at temperatures below freezing. The MVD can range from 10 microns to 50 microns for supercooled droplets, and is much larger, on the order of one millimeter, for freezing rain.

1.2. Rime vs. Glaze Ice

Based on the icing cloud conditions, the shape, and velocity of the accreting body, two general categories of ice, rime ice and glaze ice, can be formed (Fig. 1-1).

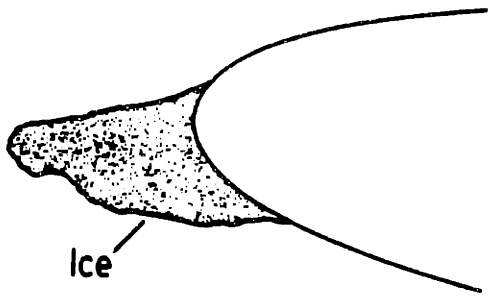

a. Rime ice accretion

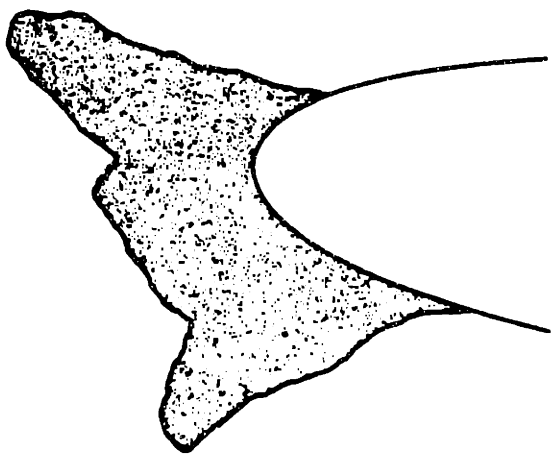

b. Glaze ice accretion

Fig. 1-1 Examples of rime ice and glaze ice, [from Ref. 1].

Rime ice is a dry ice growth, which is formed when there is sufficient heat transfer to remove all the latent heat of freezing of incoming water, and the impinging water is frozen upon impact. Rime occurs at relatively low LWC and/or cold temperatures, where the heat transfer is high and the impinging water mass is small. For this case, the freezing fraction, defined as the ratio of frozen mass to the total impinging water mass, is unity. Ice accretion modeling is relatively simple in the rime ice regime, since the droplets freeze on impact and the problem is reduced to calculating the distribution of the impinging water mass. The techniques for determining droplet trajectories are well accepted and the ability to predict rime ice accretions is limited primarily by the ability to adequately model the flow field.

Glaze ice is formed when there is an insufficient heat transfer to freeze all impinging droplets. For these cases, the accretion is controlled by the convective heat transfer (i.e. the ability to remove the latent heat released by the freezing water). Therefore, it is necessary to consider both the energy balance and the impinging mass flux in order to correctly predict glaze ice accretions. The modeling of glaze ice is significantly more difficult than for the rime ice, because the convective heat transfer is a function of both the flow field and the surface roughness size.

1.3. Current Ice Accretion Prediction Techniques

The LEWICE ice accretion prediction code, developed by NASA Lewis Research Center is representative of current icing modeling techniques. Its analytical results have been compared to experimental ice accretion results. It has been found that LEWICE can often correctly predict rime ice accretion as shown in Fig. 1-2.

However, for glaze ice, the analytical results are not always consistent with the experimentally observed results. One of the causes for the erratic manner in which glaze

ice is predicted, is surface roughness. An example of the effect of roughness on the accreted ice shape can be found in Fig. 1-3. Varying the roughness is observed to significantly alter the predicted ice shapes.

Although the roughness input plays an important role in computing the shape of glaze ice accretions, the determination of the roughness size is based on an empirical formula, derived from a limited data set. The input roughness values are calculated based on the icing cloud conditions, and do not correspond to the experimentally observed roughness sizes for some cases. The empirical manner in which the roughness parameter is used suggests that more deterministic treatment of roughness is necessary, in order to improve glaze ice accretion.

Another discrepancy is that although the surface roughness is assumed to be uniform for the entire surface in LEWICE, different surface roughness zones had been observed on glaze ice accretion by Hansman and Turnock[4]. This suggests that the use of roughness in LEWICE needs to be investigated.

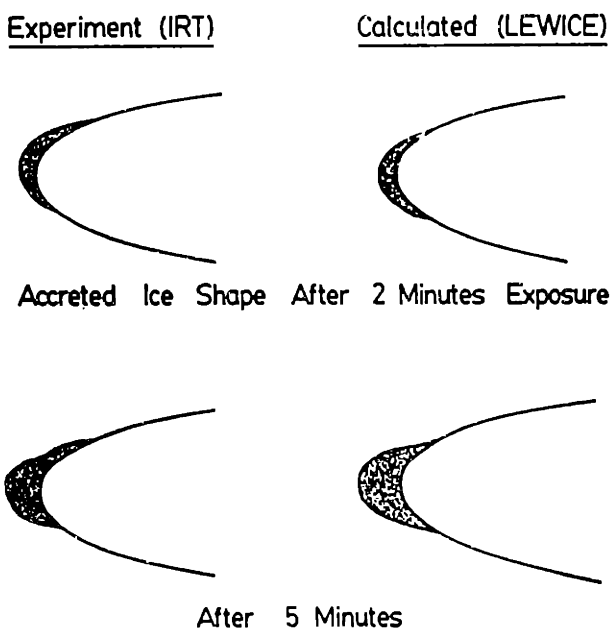

Fig. 1-2 Rime ice prediction (T = -2.61°C, V = 52.1 m/s, LWC = 1.02 g/m^3, MVD = 12 microns), [from Ref. 2].

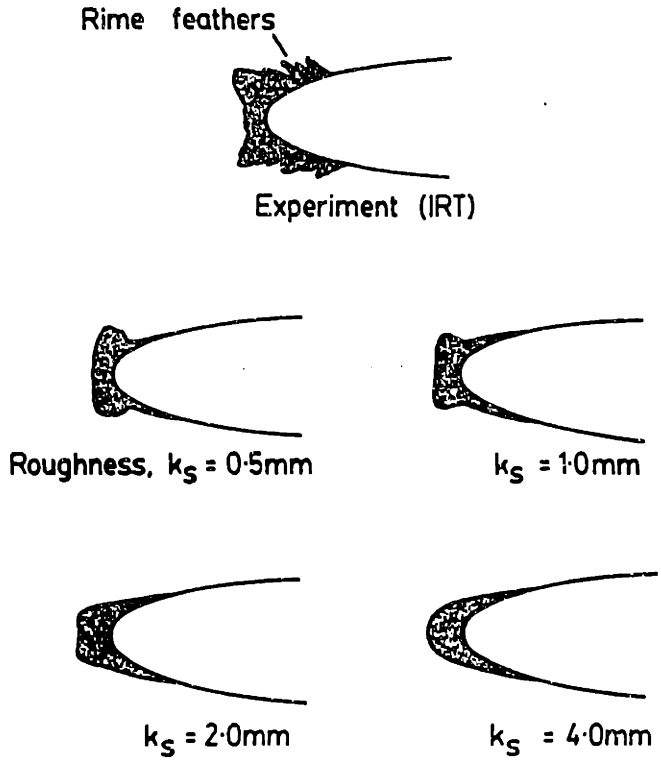

Fig. 1-3 Glaze ice prediction (T = -4.5°C, V = 77.17 m/s, LWC = 1.0 g/m^3, MVD = 30 microns), [from Ref. 3].

1.4. Motivation for research

The goal of this thesis is to analyze the cause for the erratic performance of the current ice accretion prediction techniques in the glaze ice regime and introduce modifications to improve ice prediction.

In an effort to determine the cause for the discrepancies between analytical predictions and experimental results, the LEWICE ice accretion prediction code was examined in detail. In particular, the thermodynamic calculation routine was analyzed, focusing on the effects of the input roughness parameter. The calculated heat transfer coefficient values were compared to the experimentally measured heat transfer coefficients for cylinders with known roughness element heights.

Experiments were conducted in various icing tunnels to obtain a data base for comparison with the analytical results. Based on experimental observations, hypotheses concerning surface roughness and surface water behavior were made, and a simple modification to the current technique, Multi-Zone model was proposed. To determine the effectiveness of the Multi-Zone model, it was implemented in the LEWICE code, and the results were compared with the experimentally observed ice shapes.

2. LEWICE Ice Accretion Prediction Code

LEWICE is an interactive ice accretion prediction code, which was first developed at University of Dayton Research Institute and then by Sverdrup Technology, Inc. under contract from the NASA Lewis Research Center. It is widely used for commercial and military applications, to predict ice accretions on various airfoils for aircraft and helicopter design, development, and certification.

LEWICE and other similar codes are capable of accurately predicting ice accretion for certain icing conditions (Fig. 1-2). However, they are erratic in modeling glaze ice accretion. It has been observed that for the same icing condition, different value of roughness sizes result in completely different glaze ice shapes (Fig. 1-3). Because of the sensitivity of accreted ice shapes to roughness and the inability of researchers to come up with generally valid roughness correlations, it appears that there is some question as to the use of roughness in LEWICE. In order to determine the cause for this erratic performance, the structure of LEWICE is described below in detail.

2.1. Structure of LEWICE

The general structure of the analytical code with multiple time steps is shown in Fig. 2-1. LEWICE consists of three major modules: the flow field calculation, the particle trajectory and impingement calculation, and the thermodynamic and ice accretion calculation. First, the flow field around an arbitrary 2-dimensional body is calculated. Then, based on that flow field, the droplet trajectories are calculated. The droplets are released form a region upstream of the body, and the location of droplet impingement is determined. The local ice accretion rate is then determined based on the impinging water mass and the convective heat transfer. The new ice shape is calculated, the time step is incremented, and the procedure is repeated for the next time step.

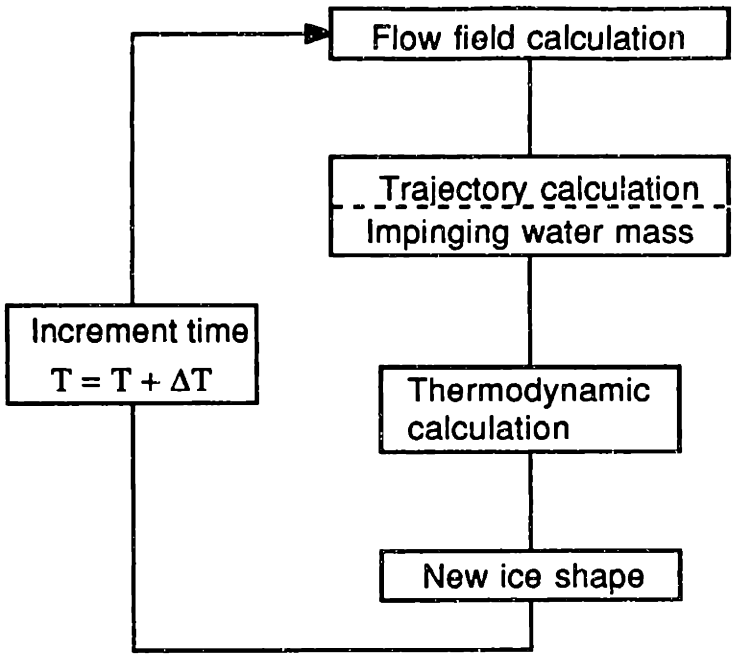

Fig. 2-1 General structure of an analytical code LEWICE.

2.1.1. Flow Field Calculation

The flow field calculation module uses the two-dimensional potential flow program developed by Hess and Smith.[5] The input parameters for the flow calculation includes the coordinates of the body, the angle of attack, and several computational parameters. The potential flow field (inviscid, incompressible) around an arbitrary body, which is defined by a set of segments, is described by a distribution of sources, sinks, and/or vortices along the body surface. With this method, it is theoretically possible to calculate a flow field around a irregular, convoluted ice shapes that occur with many icing conditions. The stagnation point is determined by checking the surface velocities for a change in sign. This comes from the assumption that the velocities on the lower surface are negative and those on the upper surface are positive. However, with this method, there is a problem of having multiple stagnation points. This problem is solved in LEWICE by having the user pick an

appropriate point interactively as the stagnation point based on the geometry of the accreting body.

2.1.2. Droplet Trajectory Calculation

Based on the non-dimensional velocity calculated in the flow field routine and the input parameters which define the icing condition, such as LWC and MVD, the trajectories of the impinging droplets are calculated. The droplet trajectory calculation simulates the motion of the impinging water droplets around an arbitrary body using the equations of motion for a point mass particle in a potential flow field.[6] The impinging water droplets are assumed to be rigid spheres with known diameters. A distribution of the droplet sizes can be input, but typically, the code is run with a single diameter, typically as MVD size, in order to shorten the computation time. The only forces considered to be acing on the particles are those of drag and gravity. The equations of motion are integrated using the method of Gear developed for stiff equations.[7,8] The droplet impingement is calculated based on the droplet trajectory, by determining whether the droplet hits the body or goes out of a user specified range. Based on these calculations, the local collection efficiencies, defined as the ratio of the mass flux of droplets arriving at a point on the surface and the mass flux of the droplets which would pass through that position in an undisturbed flow, along the surface of the body are calculated.

2.1.3. Ice Accretion Calculation

The thermodynamic characteristics of the freezing process on a body undergoing icing are calculated by considering the mass and energy balance for control volumes located on the surface. (The mass and energy balance equations are presented in Appendix A.) A control volume is defined to be of unit depth, along a segment, with height greater than the boundary layer thickness (Fig. 2-2). Based on the heat balance and the mass flux, the freezing fraction for each control volume are determined. These, coupled with droplet

impingement calculations, determine the amount of ice formed for each of the control volumes.

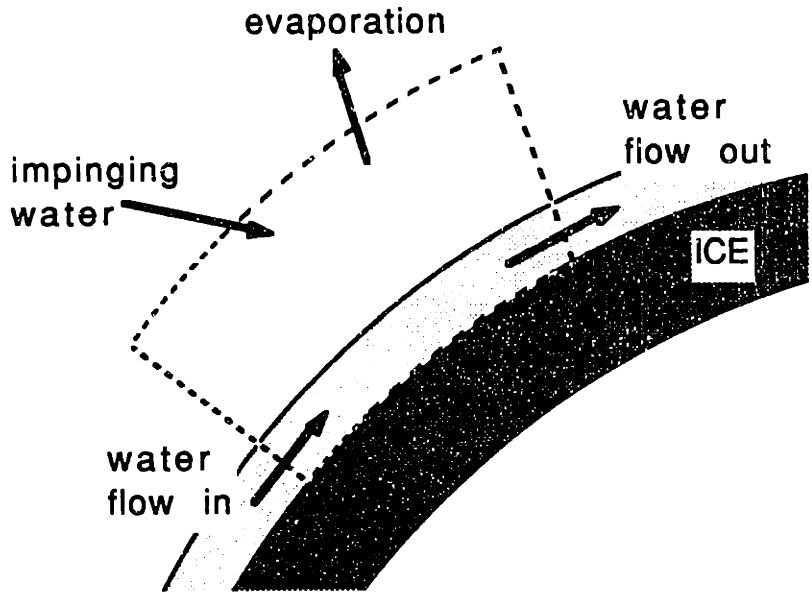

Fig. 2-2 Schematic description of a control volume and mass balance.

The ice accretion rate calculation utilizes a Messinger mass balance model.[9] In this model, the surface roughness is assumed to be uniform, and an effective equivalent sand grain roughness, k_s, is input to the code. It is assumed that a certain fraction of the impinging water is frozen, and that all unfrozen water runs back along the surface. This unfrozen water then becomes the impinging water mass at downstream points.

The freezing fraction is determined by the energy balance for each of the control volumes. The heat balance for a control volume is shown in Fig. 2-3. There are seven components that contribute to the energy balance in an icing situation. Of these, energy carried by the impinging water and water runback flow, and the heat released by the freezing water represent the energy flow into the control volume. The other four components represent the energy flow out of the control volume. Of these four energy

transfer mechanisms out of the control volume, convection is the most important. Because the convection dominates the heat removal mechanism, the ice accretion rate depends heavily on convection. Therefore, the convective heat transfer rate, h_c, which is related to the convective heat flux, q, by:

$$q = h_c (T-T_{surf}) \qquad [2\text{-}1]$$

where T is the freestream temperatures and T_{surf} is the surface temperatures, has a major impact on the ice accretion rate and in many cases is the controlling parameter. The details of the heat transfer computation is described in the next Section.

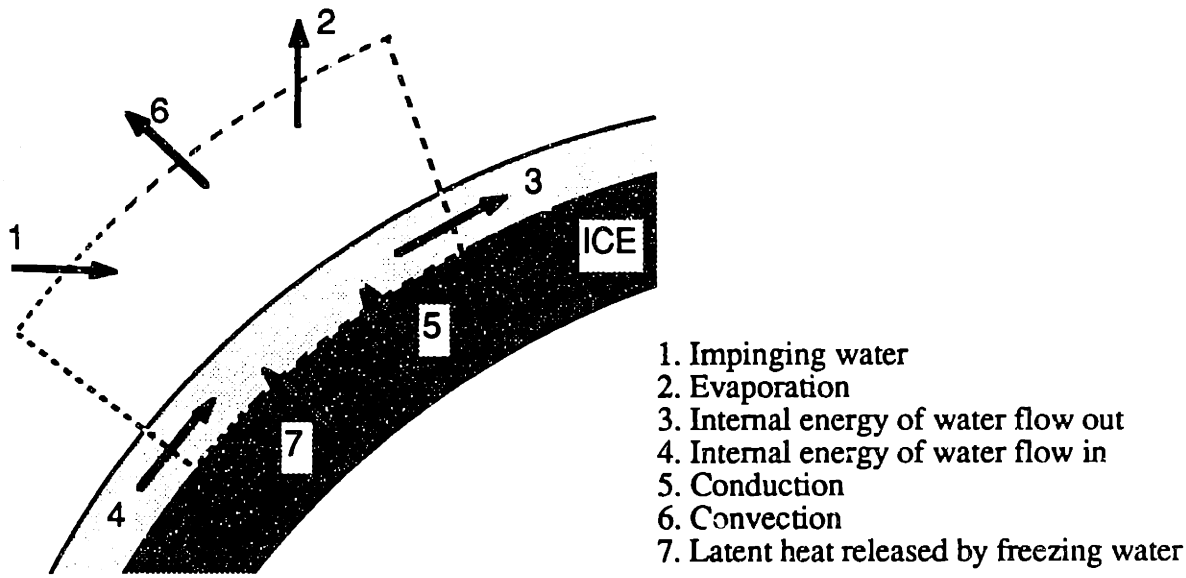

Fig. 2-3 Schematic description of heat balance for a control volume.

For ice accretion predictions involving multiple time steps, the user has an option to re-calculate the flow field around the accreted body or use the flow field from the previous time step. Then, the thermodynamic and ice accretion calculation is repeated for the next time step.

2.2. Use of Roughness in LEWICE

The only roughness parameter currently input to LEWICE is the equivalent sand grain roughness height, k_s. This parameter has been shown to be one of the most important factors in determining the ice shape in glaze as shown in Fig. 1-3.[10,11] In current ice accretion models, the value for this roughness parameter is assumed to be uniform for the entire surface and is determined empirically, by comparing the predicted ice shapes to the experimental results. When the experimental shape is not available for comparisons, a method for calculating an appropriate value is suggested, based on past comparison between the predicted ice shape and the experimental results. For LEWICE, the empirical relations were based on a series of experiments and comparisons conducted for NACA 0012 airfoil.[6]

Physically, rougher surface causes the boundary layer to transition earlier, and results in higher heat transfer in the turbulent region. Therefore, the roughness parameter

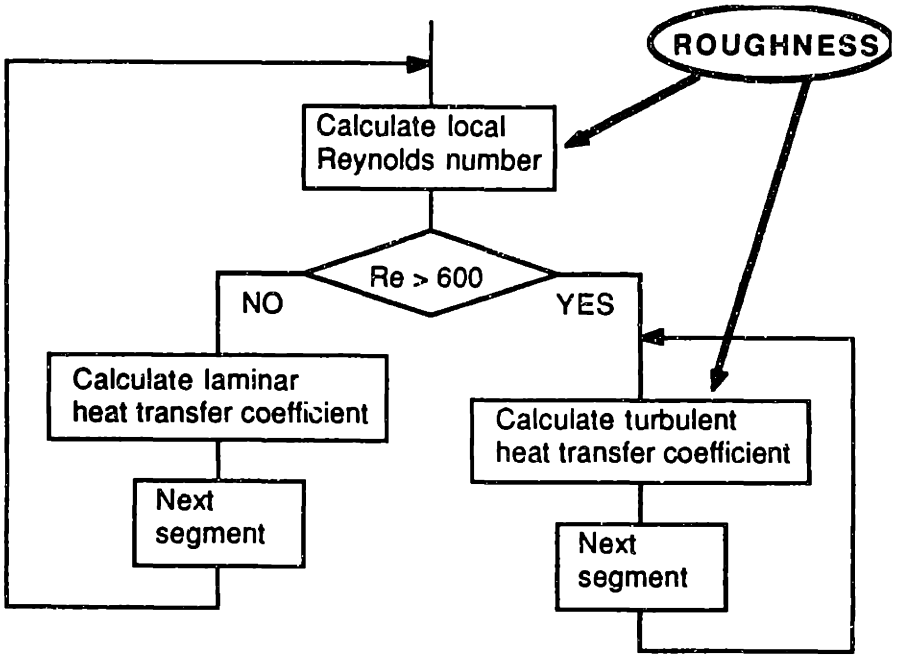

Fig. 2-4 Use of roughness in heat transfer calculation.

is used in two ways in LEWICE. One use is to determine the location of transition from laminar to turbulent boundary layer and the other is to calculate the heat transfer coefficient in the turbulent region as shown in Fig. 2-4. These two uses will be described in detail below.

2.2.1. Boundary Layer Transition Location

Rougher surface causes the boundary layer transition to occur earlier. This is modeled with reference to a critical Reynolds number based on the roughness element height and local velocity. The local Reynolds number based on roughness element height is:

$$Re_l = \frac{k_s u_k}{\nu} \qquad [2\text{-}2]$$

where k_s is the roughness element height in the laminar region, u_k is the velocity at distance k_s from the surface, and ν is the kinematic viscosity. When the local Reynolds number exceeds an empirically determined critical roughness element Reynolds number of 600, the

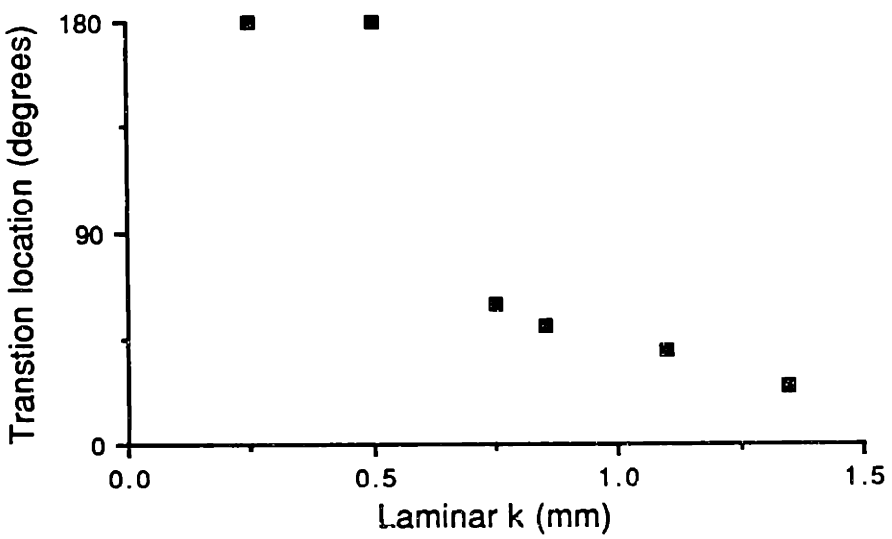

Fig. 2-5 Effect of k_s in the laminar region on the transition location (T = 0°C, V = 24.27 m/s).

boundary layer is transitioned from laminar to turbulent,and any region downstream of this point is considered to have turbulent boundary layer.[12] The detailed calculation is discussed in Appendix C. The effect of varying k_s in this region on the transition location is demonstrated in Fig.2-5 by running LEWICE for several values of k_s at a velocity of 24.27 m/s and temperature of 0°C for a 0.15 m cylinder. It can be seen that no transition takes place until some minimum value of k_s between 0.5 mm and 0.85 mm at which point the transition location propagated towards the stagnation region with increasing k_s.

2.2.2. Calculation of Turbulent Heat Transfer

In the laminar region, the heat transfer is independent of the roughness element height, with the assumption that the roughness height is less than the boundary layer thickness. In regions with a turbulent boundary layer, the roughness element height becomes important. Here, the heat transfer coefficient increases with surface roughness. The heat transfer coefficient calculation in the turbulent region involves a set of very

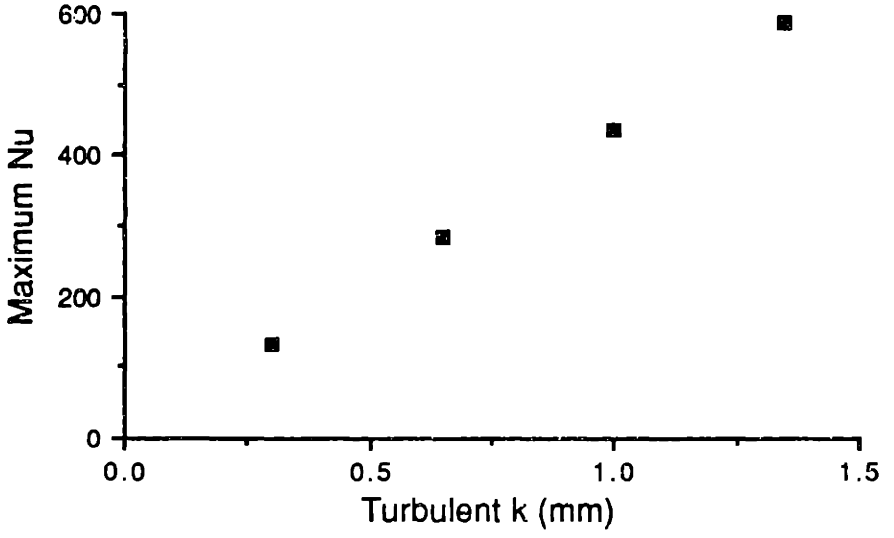

Fig. 2-6 Effect of k_s in the turbulent region on the magnitude of the maximum heat transfer coefficient (T = 0°C, V = 32.93 m/s).

complicated equations based on flow parameter and geometries of the accreting body, including roughness element height.[6] Because of the complexity of these equations, (shown in Appendix C) it is very difficult to analytically determine the effects of k_s on the turbulent heat transfer analytically. However, the effects of k_s on heat transfer in the turbulent boundary layer can be observed numerically using LEWICE. An example is shown in Fig. 2-6 where the maximum heat transfer is plotted as a function of roughness element height, for a 0.15 m cylinder at a velocity of 32.93 m/s and temperature of 0°C. It was found that increasing k_s significantly increased the maximum heat transfer in the turbulent region.

2.3. Implementation of LEWICE at M.I.T.

In order to facilitate analysis and modification of LEWICE, it was necessary to install a version of LEWICE on a VAX computer at M.I.T. LEWICE is an interactive program, which requires user input at several points in the computational cycle. It has graphic routines, which make it easier for the user to asses the icing situation and enter the necessary input, as well as provide hard copy of the data. However, the graphic routines for the original version of LEWICE were written using an in-house graphics package at NASA Lewis Research Center. Modifications were required in order to utilize these routines at M.I.T. With the assistance of the FAA Tech Center, a version of LEWICE compatible with VAX machines was obtained, and several modifications were made such that the program ran smoothly on a M.I.T. Micro VAX.

In order to convert the plotting routines, several subroutines were added to LEWICE, which linked the plot calls from the original LEWICE to a graphics package available at M.I.T. This enabled the user to perform much of the interactive and graphical routines present in the original LEWICE code.

2.4. Corrections to LEWICE

While analyzing the code, it was found that there were several errors in the LEWICE code. Therefore, corrections were introduced into LEWICE.[13]

2.4.1. Viscosity

After a detailed analysis of the thermodynamic calculation routine, it was noted that the calculation of the kinematic viscosity, ν, was not accurate, when compared to the known values of that for air. The formula for the calculation of the kinematic viscosity was replaced by a more accurate Sutherland formula for kinematic viscosity:[14]

$$\nu = \frac{\mu_0}{\rho}\left[\left(\frac{T}{T_0}\right)^{1.5}\frac{T_0+S}{T+S}\right] \qquad [2\text{-}3]$$

where S is the Sutherland constant for kinematic viscosity of 199, μ_0 is the dynamic

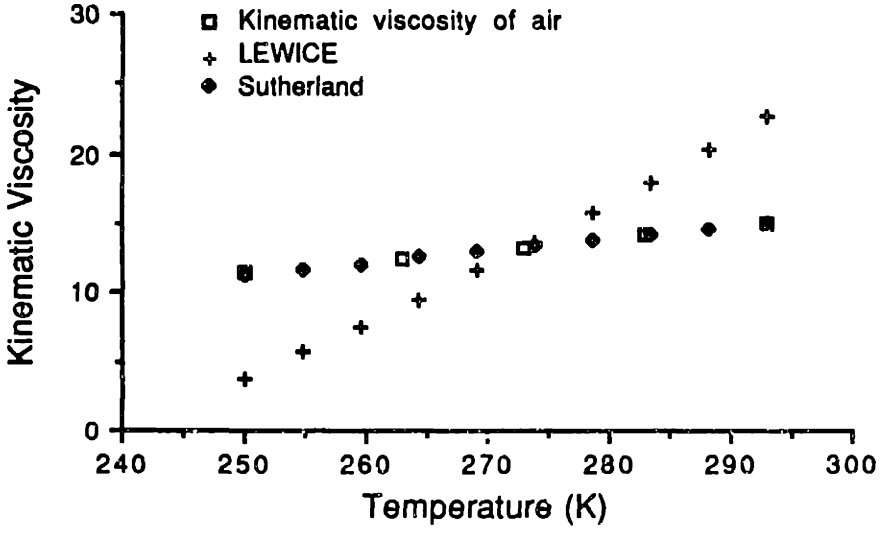

Fig. 2-7 Comparison of viscosity vs. temperature for original and modified LEWICE and experimental values.

viscosity, ρ is the density of air, and T_0 is the reference temperature of 491.6°R. The result is shown in Fig. 2-7, where the kinematic viscosity calculated by the algorithm used in the original LEWICE and by Sutherland formula are compared to the known values of kinematic viscosity for air.

2.4.2. Thermal Conductivity

To be consistent with more rigorous calculation of the kinematic viscosity, the formula for the calculation of thermal conductivity as a function of temperature was also replaced by a Sutherland formula for thermal conductivity:[14]

$$\frac{k}{k_o} = \left(\frac{T}{T_o}\right)^{1.5} \frac{T_o+S}{T+S} \qquad [2\text{-}4]$$

where S is the Sutherland Constant for thermal conductivity of 199, k_0 is the reference thermal conductivity for air of 0.0241 W/m°K and T_0 is the reference temperature of 491.6°R. This allowed for greater accuracy for wider range of temperatures.

2.4.3. Surface Distance

It had been found previously[10] that in LEWICE the surface distance for the new ice layer is not computed in the same time step in which all the other icing parameters are computed. The surface distance is defined as the distance from the stagnation point to the midpoint of segments which define the accreting body, along the surface of the body. This parameter is used to indicate the position along the surface. It is used for plotting different parameters. Therefore, it is important for this parameter to be calculated in the same time step as the other parameters, and the change was implemented.

2.4.4. Multiple Stagnation Points Resolution Routine

One of the options available on VAX computers is to run the programs in batch mode, where a series of programs can be executed using one command. In order to utilize this option, it is necessary that all inputs normally provided by the user be stored in a file, and that all inputs be known prior to running the program. However, in the original LEWICE, if multiple stagnation points were calculated during flow field calculation, the user was asked to examine the locations of these points and choose a point most appropriate for that situation. Therefore, in order to run the program in batch mode, it was necessary to pr ide the program with a method for determining the most appropriate stagnation point.

This task had been attempted by the FAA Technical Center, whose method was to choose as the stagnation point a point closest to the stagnation point calculated in the previous time step. However, it was found that this method did not always choose the correct stagnation location for the cases run. Because most of the cases run for heat transfer study were for symmetrical body at 0° angle of attack, a new routine was written, where for a symmetric body at zero angle of attack, the point with minimum distance to the line of symmetry was chosen as the stagnation point. This routine provided a more accurate method for determining stagnation points.

3. Heat Transfer Coefficient Comparison

Because the heat transfer plays a critical role in determining the glaze ice accretion, the heat transfer coefficients predicted by LEWICE were compared against experimental data. The experimental data consisted of heat transfer coefficient measurements on cylinders with known roughness heights taken by Achenbach.[15] By comparing the heat transfer coefficients, the effectiveness of the roughness input parameter, k_s, and the thermodynamic calculation method used in LEWICE can be evaluated.

3.1. Heat Transfer on Cylinders

A typical LEWICE prediction of heat transfer coefficient versus angular position for a circular cylinder is shown in Fig. 3-1a. The θ on the x-axis refers to the angular position on the surface measured from the stagnation point (Fig. 3-1b). The heat transfer coefficient is expressed as a normalized value:

$$\text{Normalized HTC} = \frac{Nu}{\sqrt{Re}} \qquad [3\text{-}1]$$

where Re is the Reynolds number based on freestream velocity, and Nu is the Nussult number defined as:

$$Nu = \frac{h\,x}{k} \qquad [3\text{-}2]$$

where h is the heat transfer coefficient, x is the characteristic length (diameter of the cylinder), and k is the thermal conductivity of air.

The heat transfer plot typically has a relatively constant magnitude around stagnation region ($\theta = 0$). This corresponds to the region of laminar boundary layer with laminar heat transfer. At some point downstream, there is a sudden rise in the magnitude of the heat transfer, where the boundary layer transitions to turbulent. Aft of this point, the

heat transfer is that for turbulent boundary layer. Here, the flow field and surface roughness play an important role in the calculation of the heat transfer, and the magnitude varies with the velocity field, resulting in a maximum to occur at about 90°.

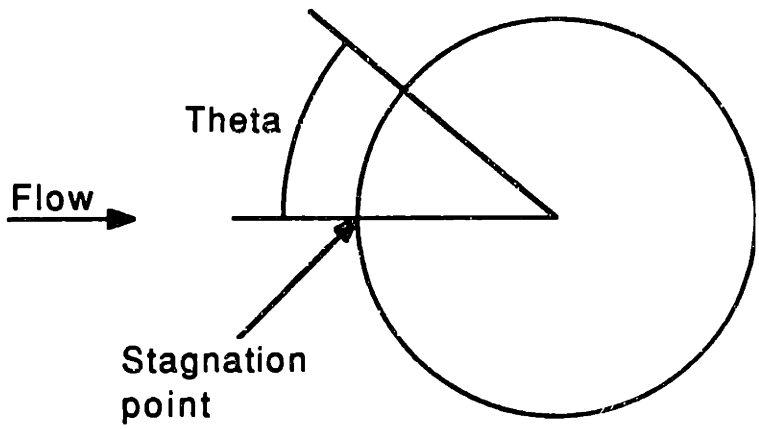

a. Notation used for the heat transfer coefficient comparisons on cylinders.

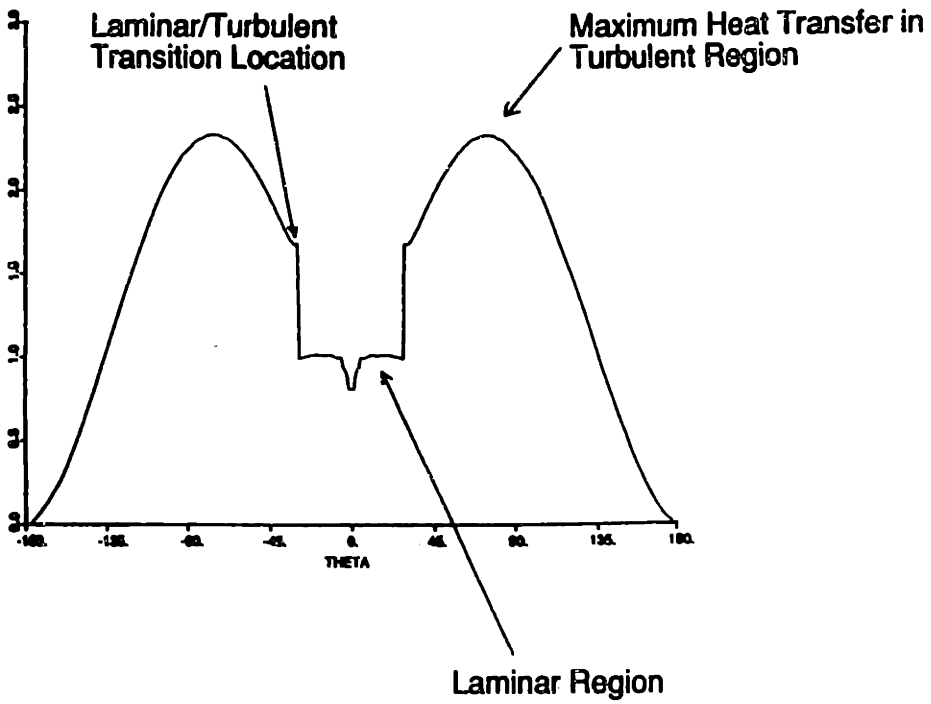

b. Typical heat transfer versus angle plot.

Fig. 3-1 Heat transfer on cylinders.

3.2. Achenbach Experimental Data

The experimental heat transfer coefficient data of Achenbach consists of measurements taken on rough 0.15 m diameter cylinders.[15] The roughness elements on the cylinders were manufactured by knurling the surface of the cylinders, resulting in roughness which were regular arrangements of pyramids, each having a rhomboid base. Three different roughness element heights, with known equivalent sand grain roughness heights of 0.115 mm, 0.45 mm, and 1.35 mm, were tested. The measurements provide heat transfer coefficient data for cylinders with known surface roughness sizes at various Reynolds numbers.

3.3. Implementation in LEWICE

Since no ice was accreted for these comparisons, it was only necessary to run LEWICE for a single time step. Because the equivalent sand grain roughness sizes are known, eliminating the uncertainty in the input roughness parameter, the effectiveness of the heat transfer calculation routine can be assessed by comparing the calculated heat transfer to the experimental data.

By comparing the predicted and experimental boundary layer transition location, the validity of the critical Reynolds number of 600 was tested. In LEWICE, the boundary layer is assumed to be turbulent when the local Reynolds number exceeds the critical Reynolds number value of 600. Therefore, knowing the velocity at the experimental transition location and the roughness element height, k_s, the Reynolds number needed to predict the correct transition point can be calculated from the definition of the local Reynolds number based on roughness:

$$Re_1 = \frac{k_s \, u_k}{\nu} \qquad [3\text{-}3]$$

where k_s is the equivalent sand grain roughness element height, u_k is the velocity at k_s distance from the surface, and ν is the kinematic viscosity.

The validity of the turbulent heat transfer model used can be assessed by comparing the magnitude of the heat transfer in the turbulent region.

3.4. Transition Location

A typical heat transfer comparison is shown in Fig. 3-2 for a case with Re = 1.27 x 10^5 and a moderate roughness element size ks of 0.45 mm. In this case, the heat transfer is well predicted in the laminar region. However, where the transition to a turbulent boundary layer is indicated by a rise in the Achenbach heat transfer data at 75°, LEWICE predicts transition further forward at 57°. This discrepancy can be explained by a hypothesis that the transition model, based on the critical roughness element Reynolds number of 600 is not valid for this case. The critical Reynolds number needed for this case was 975.

Another comparison is shown in Fig. 3-3 for a case with Re = 5.9 x 10^5 and a small roughness element height of 0.115 mm. Here, LEWICE does not predict transition to turbulent at all, where the experimental result indicate a transition at 63°. For this case of very small roughness element size, the transition model is clearly not valid, since it fails to predict transition at all, indicating the limit of the critical transition Reynolds number criterion.

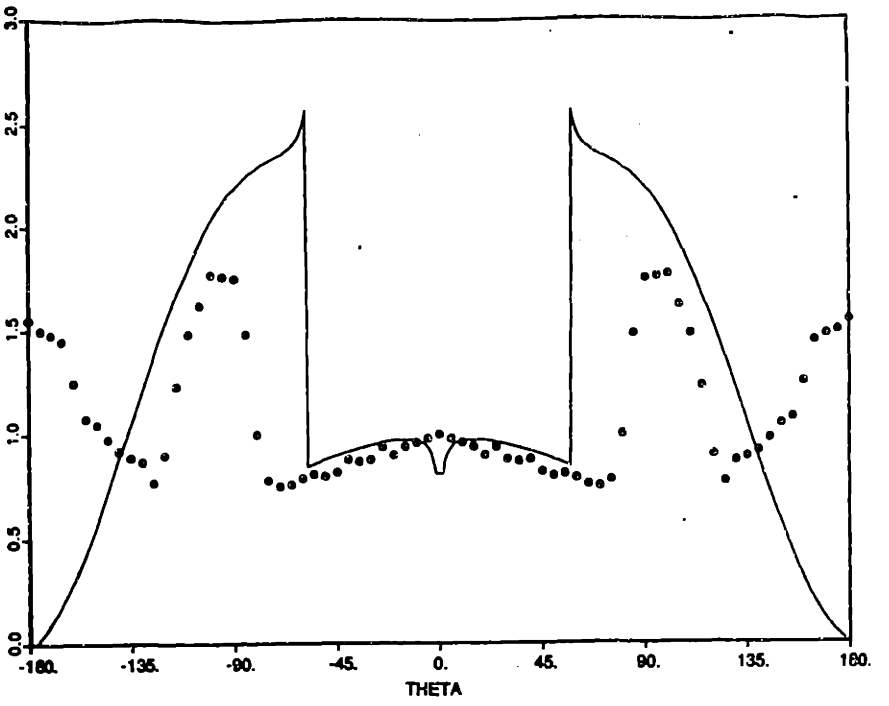

Fig. 3-2 Comparison of normalized heat transfer coefficients (Re = 1.27 x 10^5, k_s = 0.45 mm)

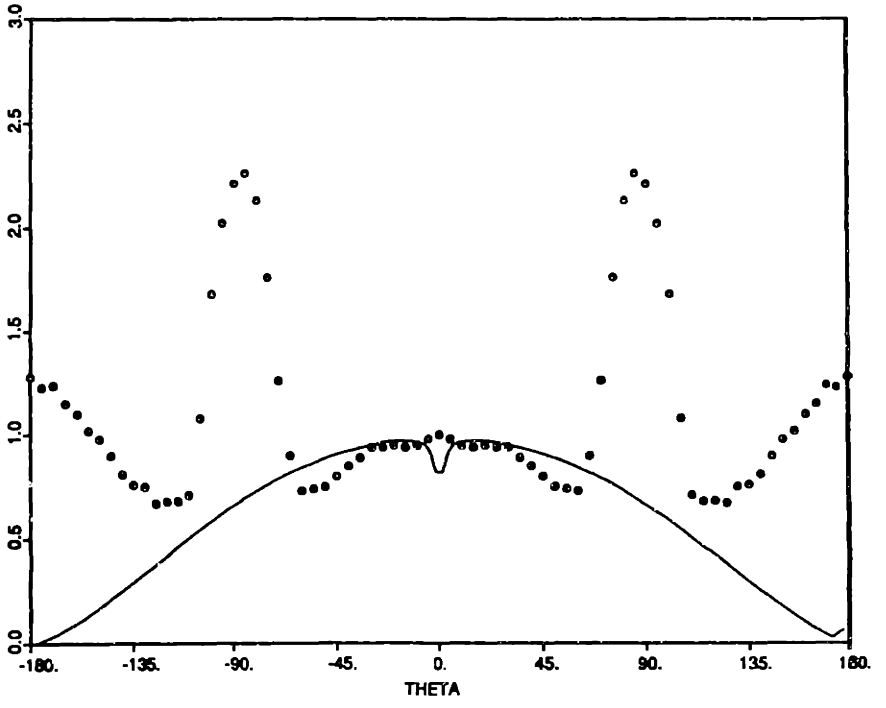

Fig. 3-3 Comparison of normalized heat transfer coefficients (Re = 5.9 x 10^5, ks = 0.115 mm).

Table 3-1 shows the locations of transition points indicated by the experimental results and LEWICE predictions for different roughness element heights. It was found that for the small surface roughness element size, LEWICE tended to not predict transition, where as for the large roughness element size, LEWICE tended to predict transition closer to the stagnation region than the experimentally observed locations. For the moderate roughness element size of 0.45 mm, LEWICE predicted the location of transition relatively well, however, it should be noted that even for these cases, the difference was as high as 20°. The critical Reynolds number needed for each case is also summarized in Table 3-1. When no transition was observed in experimental results, the maximum value of Reynolds number calculated is shown, indicating that critical Reynolds number must be larger than these numbers in order not to predict transition.

For medium size of 0.45 mm, the current criterion works well. However, for the large roughness size of 1.35 mm, the critical Reynolds number of 600 clearly is too small, where for the small roughness size of 0.115 mm, the critical Reynolds number is too large. However, these results indicate a significant scatter, indicating that caution should be used in determining the most effective method for determining the transition location.

3.5. Magnitude of Turbulent Heat Transfer Coefficient

The comparisons in Fig. 3-2 and 3-3 indicate that the magnitude of the heat transfer coefficient predicted do not always agree with the experimentally observed values, especially in the turbulent region. This problem was investigated by comparing LEWICE predicted and experimentally observed maximum heat transfer coefficient in the turbulent region. Fig. 3-4 shows the predicted and observed maximum heat transfer coefficient, as a function of Reynolds number, for large roughness element size of 1.35 mm and Fig. 3-5 for the medium roughness element size of 0.45 mm. These results indicate that the error

increases with Reynolds number, but shows different trends for the two roughness element heights.

Table 3-1 Summary of angular locations of transition and critical Reynolds number for Achenbach data.

Re	ks [mm]	Experimental transition location [degs]	Calculated transition location [degs]	Critical Re
4.8×10^4	1.35	None	46	>845
7.3×10^4	1.35	50	28	975
2.8×10^5	1.35	15	6	1276
3.8×10^5	1.35	5	4	699
8.8×10^5	1.35	5	2	1350
7.2×10^4	0.45	None	None	>329
1.27×10^5	0.45	75	57	664
1.46×10^5	0.45	45	46	603
2.26×10^5	0.45	20	28	453
8.6×10^5	0.45	0	32	0
9.2×10^4	0.115	None	None	>408
1.9×10^5	0.115	80	None	105*
4.1×10^5	0.115	105	None	166*
5.9×10^5	0.115	60	None	557

* These are the local Reynolds number calculated at the experimentally observed transition location. However, using these as the critical Reynolds number will not result in correct transition location prediction, since the Reynolds number reaches its maximum value upstream of these locations with inviscid flow field.

It should be noted that part of the reason for the disagreement in the calculated and experimental heat transfer coefficients is due to the flow field effects. An example is shown in Fig. 3-6 for a case with Reynolds number of 8.6×10^5 and k_s of 0.45 mm. The calculated heat transfer coefficient is observed to maximize at about 90° where the maximum inviscid flow around a cylinder is calculated. However, the experimental results show the maximum value at about 50°. Also, in the separation region aft of the cylinder (θ>120°), the experimental heat transfer coefficient can be observed to increase. However, the calculated heat transfer does not, due to the inviscid flow field assumption.

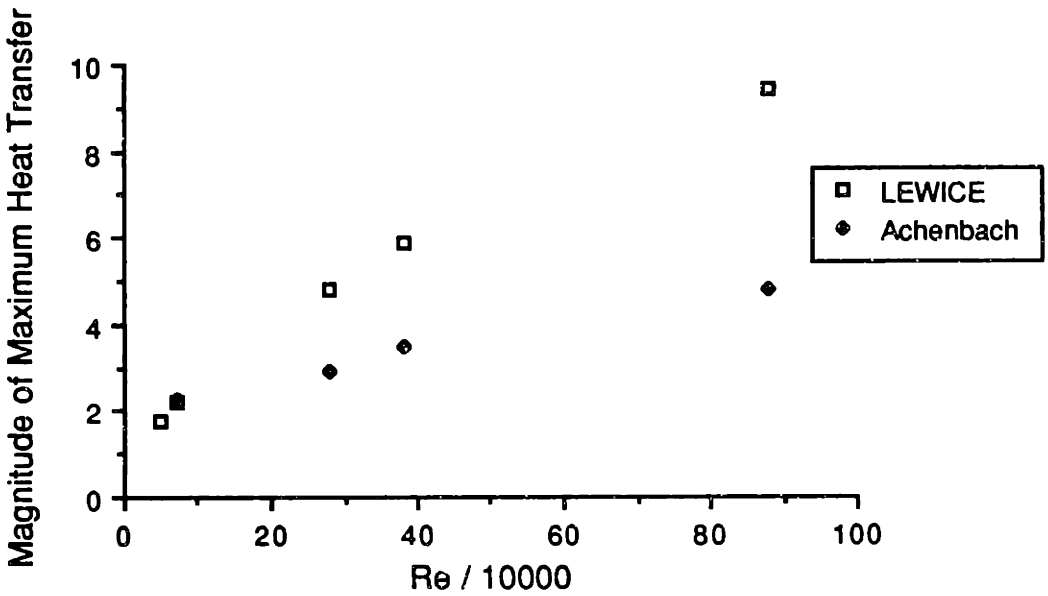

Fig. 3-4 Magnitude of maximum normalized heat transfer coefficient in the turbulent region versus Reynolds number for large roughness element size of 1.35 mm.

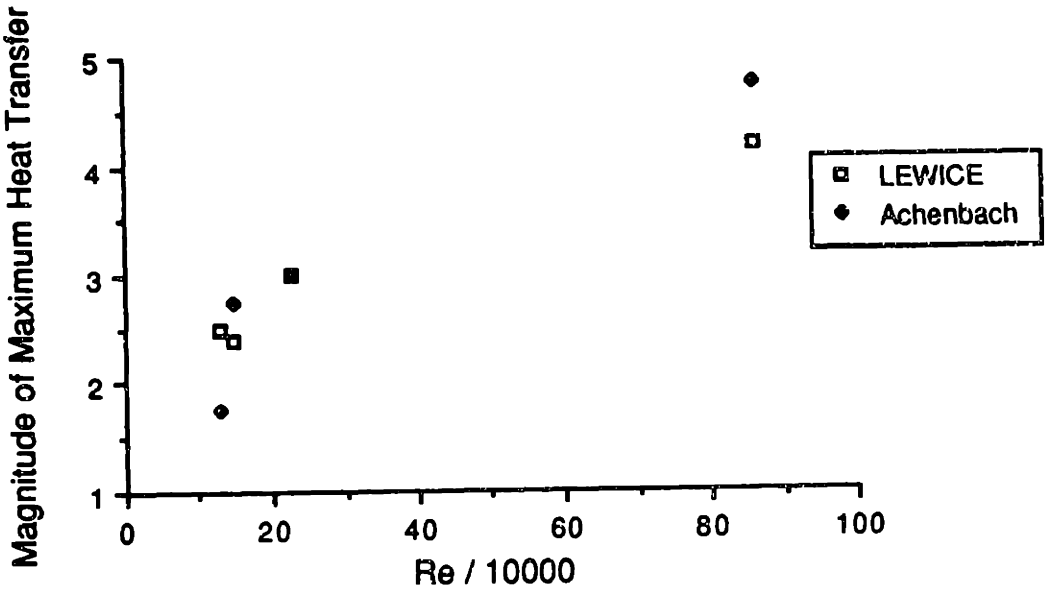

Fig. 3-5 **Magnitude of maximum normalized heat transfer coefficient in the turbulent region versus Reynolds number for medium roughness element size of 0.45 mm.**

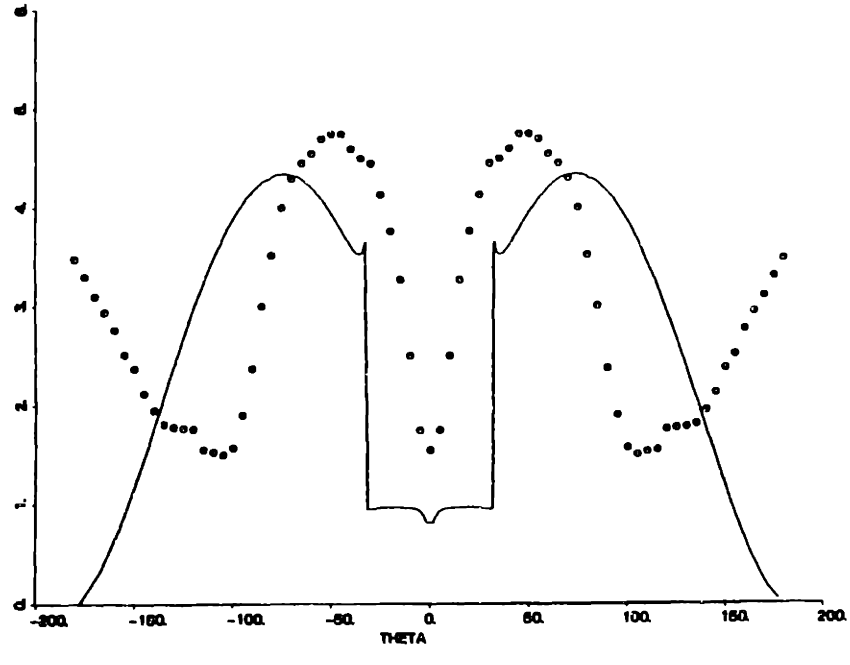

Fig. 3-6 **Comparison of normalized heat transfer coefficients (Re = 8.6 x 10^5, k_s = 0.45 mm).**

3.6. Influence of Flow field on Heat Transfer Coefficient

Because of the role the flow field plays in the calculation of heat transfer coefficient, the effect of improved flow field modeling on the heat transfer calculation was investigated. In LEWICE, the flow field around the accreting body is calculated by a potential flow code, which is inviscid and incompressible. With this method, it is impossible to calculate a flow field accurately in the separation region behind a cylinder or the recirculation region aft of a horn or glaze ice accretion. This can be observed in Figs. 3-2, 3-3 and 3-6 for a cylinder, where in the region far away from the stagnation point (θ>120), LEWICE predicts low heat transfer, where the experimental result show that heat transfer actually increases in this region. Although heat transfer in the separation region does not affect the ice shape prediction for many cases considered in icing, this result is of concern because the separation regions are observed aft of glaze ice horns, which may affect the final ice accretion shape.

Another difference between he predicted and experimental heat transfer is the location where the heat transfer curves peak. For example in Fig. 3-6, the maximum heat transfer occurs at about 90°, where the inviscid flow field has the maximum magnitude. However, the experimental result indicates the maximum heat transfer at about 60°.

In order to verify that it is possible to predict heat transfer more accurately using the LEWICE methodology with a more accurate velocity field, the potential flow field was replaced with a well-documented empirical formula for the average velocity around a cylinder:[16]

$$\frac{u_e}{V} = \left[3.6314 \frac{F_1 \theta}{2} - 2.1709 \left(\frac{F_1 \theta}{2} \right)^3 - 1.5144 \left(\frac{F_1 \theta}{2} \right)^5 \right] F_2 \qquad [3\text{-}4]$$

where V is the freestream velocity, u_e is the surface velocity, θ is the angular position from the stagnation point, and F_1 and F_2 are the constants determined experimentally. For the example case ($Re = 7.3 \times 10^4$), the values used for F_1 was 1 and F_2 was 1.11 based on experimental results, suggested by Zukauskas and Ziugzda.[16] The heat transfer was calculated using the empirical flow field and is shown in Fig. 3-7. In this comparison, because the size of the roughness element height is known, it was found that a critical Reynolds number of 975 was necessary to match the boundary layer transition location. It can be seen that the heat transfer was predicted correctly using the known equivalent sand grain roughness. The result indicates that with a viscous flow field, a more accurate prediction of boundary layer transition location and an appropriate value of roughness element height in the turbulent region, the prediction of the heat transfer can be significantly improved.

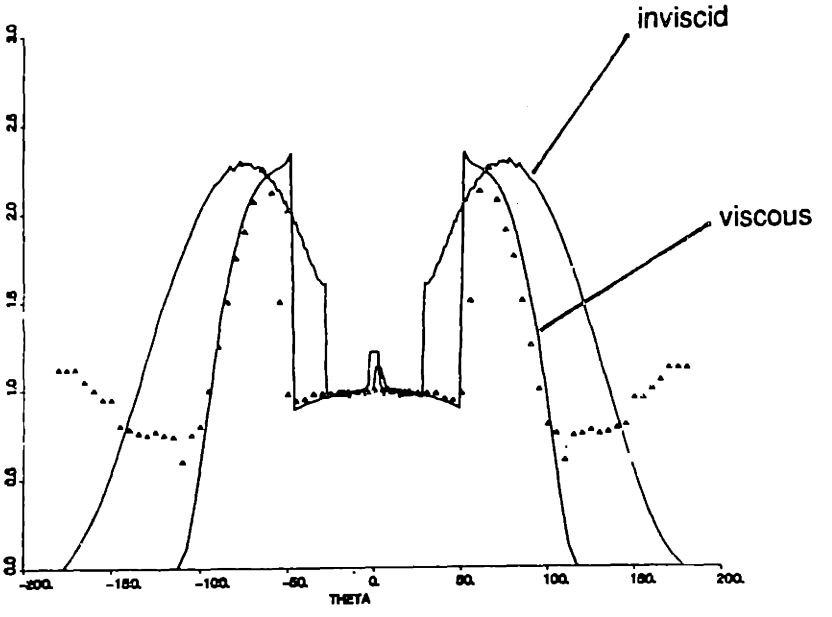

Fig. 3-7 Comparison of normalized heat transfer coefficient calculation with empirical flow field ($Re = 7.3 \times 10^4$, $k_s = 1.35$ mm)

4. Experimental Apparatus

4.1. Motivation and Objectives

In previous work by Hansman and Turnock,[4] different surface roughness zones had been observed on glaze ice accretion. It was found that glaze ice typically consisted of at least two of the three regions shown in Fig. 4-1, the smooth, rough, and the runback zones. Each of these zones were observed to have different surface roughness properties and surface water behavior. The transition between the smooth and rough zones was observed to propagate toward stagnation region as a function of time.

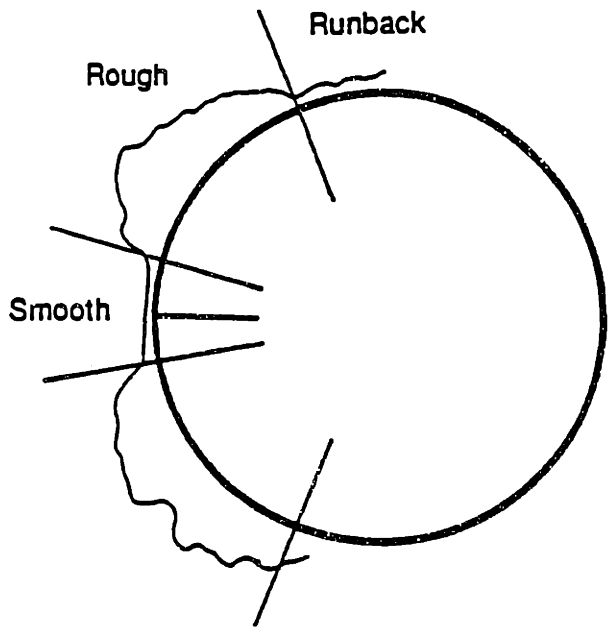

Fig. 4-1 Glaze ice accretion on a 1" cylinder showing distinct roughness regions (T = -4.5°C, V = 77.17 m/s, LWC = 1.0 g/m^3, MVD = 30 microns).

Several experiments were conducted in various icing tunnels, in order to verify prior observations of surface roughness and to obtain well defined ice shapes for comparison with LEWICE predictions. For each of the ice shapes observed, it was desired to obtain detailed observations of accreting ice surface roughness and the location of smooth to rough transition as a function of time be made through photographic and video

techniques. In addition, the surface water behavior was examined through an infrared thermal video system. The tests were conducted at the NASA Icing Research Tunnel (IRT) and the B.F. Goodrich Ice Protection Research Facility (BFGT) on several occasions.

4.2. Set-Ups and New Techniques

In both the IRT and BFGT, similar set-ups were used, focusing on observations of ice accretion on cylinders. The observations were made on 1" to 4" diameter cylinders, at freestream velocities of 51.45, 64.31, and 77.17 m/s. The liquid water content (LWC) ranged from 0.4 to 1.5 g/m^3, and the median volumetric diameter (MVD) from 11 to 40 microns. The tunnel total air temperature varied from 0°C to -15°C, with some colder runs made for calibration purposes.

4.2.1. Photographic Set-Ups

The photographic set up used in the BFGT is shown in Fig. 4-2. The test articles were cylinders which horizontally spanned the test section. The test section walls were

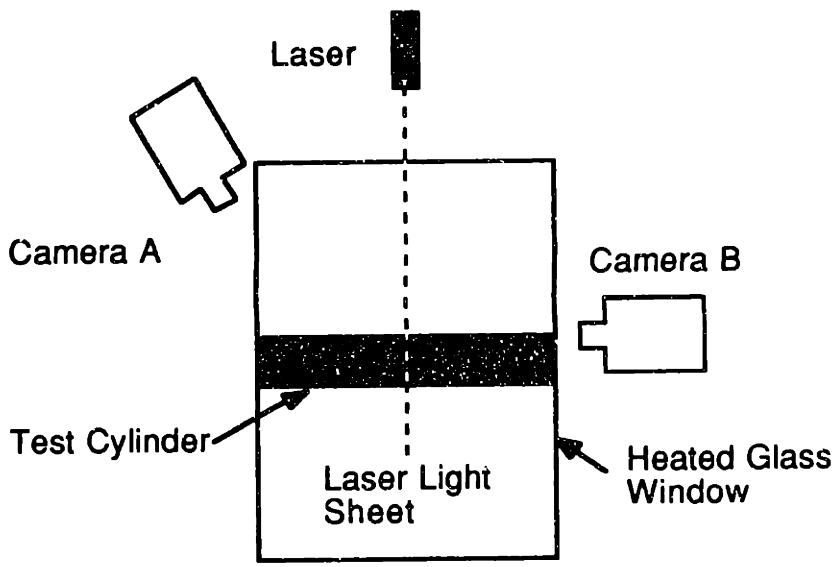

Fig. 4-2 Schematic diagram of the photographic set-up in BFGT (Camera A = normal view, camera B = grazing view).

heated glass to provide photographic access. Scale reference was provided by a grid mounted on a thin splitter plate at the midplane of the test section for some tests. The laser light sheet technique, explained in the next section, was used to illuminate a plane perpendicular to the cylinder to ease the photographic observations in BFGT. Two charge-coupled device (CCD) microvideo cameras with macrolens for magnification were used to obtain a grazing angle view of the ice accretion. For some runs, a normal view of the cylinder was also used to observe the location of smooth to rough transition. The grazing view of the cylinders provided the best ice shape photos while the normal view enabled the surface roughness observation. The cameras were focused at the cylinders in central region of the tunnel where the cloud was most uniform.

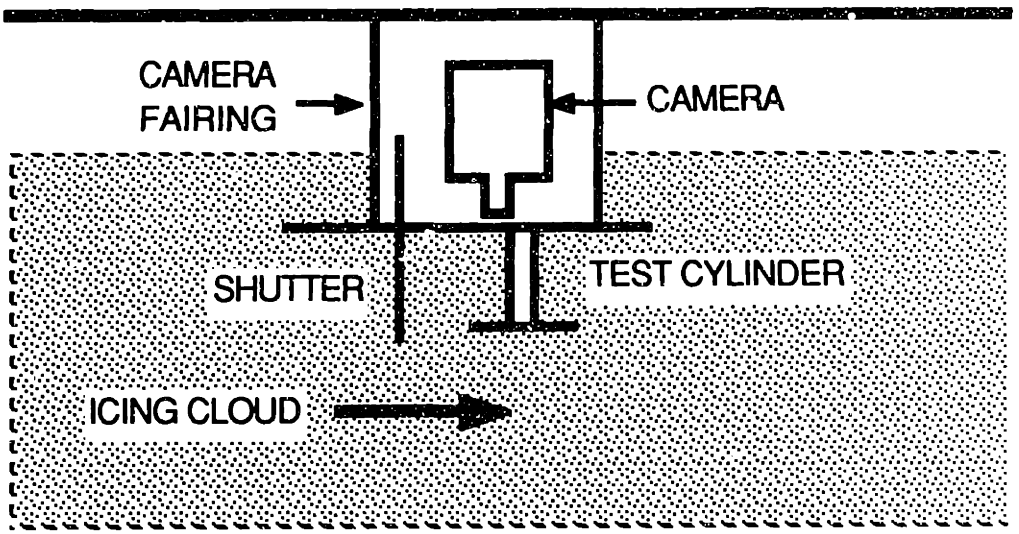

Fig. 4-3 Schematic diagram of the photographic set-up in IRT.

The photographic set-up used in the IRT tests is shown in Fig. 4-3. The photographic and test cylinder geometry is similar to the camera set-up described above for the BFGT. However, in order to locate the test cylinder within the region of uniform cloud, both the test cylinder and the camera had to be moved into the tunnel. A heated waterproof fairing was provided to protect the camera. In addition, a shutter was located

upstream to shield the test cylinder during initial transients in the liquid water content. Once the tunnel spray system had stabilized, the shield was removed and the cylinder was exposed to the icing cloud.

4.2.2. Laser Light Sheet Set-Up

For some of the tests conducted in the BFGT, a laser light sheet was used to illuminate a plane perpendicular to the test cylinders to show the plane of focus accurately (Fig. 4-4). With the laser sheet, it was possible to record on the video and still cameras, the details of accreting ice shapes and roughness at a single spanwise location. Because the rougher surface in the rough region increased the internal reflection of laser light, the ice shape appeared brighter in the rough region, improving the facility and accuracy of observation of smooth to rough transition point. The external light inside the tunnel was tuned off at a specific time interval, usually 20 seconds, which enhanced the details in the laser illuminated ice shape.

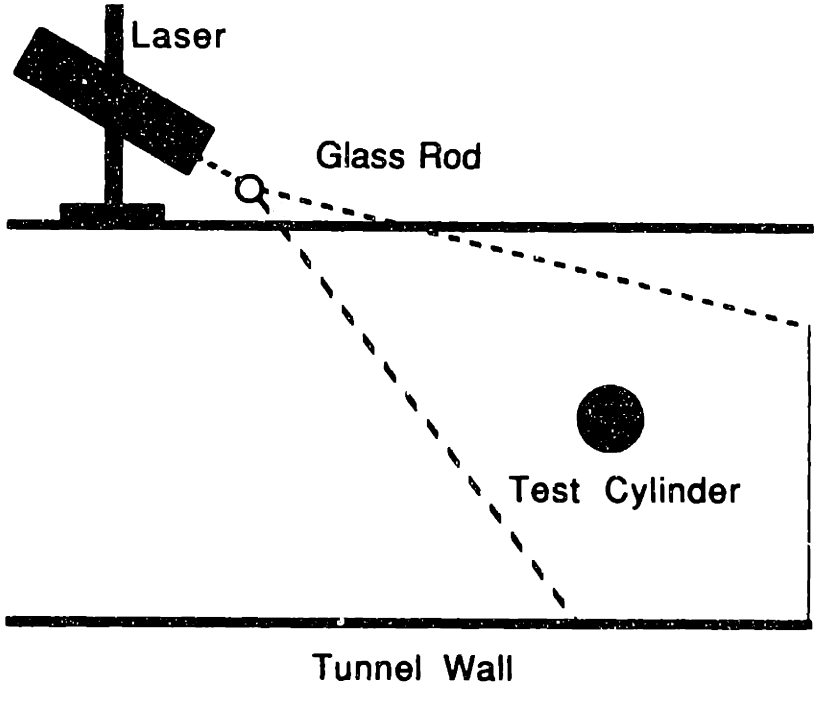

Fig. 4-4 Schematic diagram of the laser light sheet set-up in BFGT.

4.2.3. Infrared Video Set Up

The infrared (IR) thermal video system set-up was also used in the BFGT (Fig. 4-5). The IR camera was mounted above the test section, 56 cm above and 84 cm upstream of the cylinder. Because no IR transparent windows were available, a viewing slot was cut into the top of the tunnel so that the cylinder could be viewed directly. The IR video system provided color thermographs of the accreting ice surfaces and temperature profiles along designated sections. The system was typically operated with the temperature scale increments of 0.5°C and a dynamic range set between the tunnel operating temperature and 0°C. Cold air blowing out of the viewing slot cooled the IR optics and caused the absolute calibration of the system to drift. The system was, therefore, calibrated "in situ" by viewing points of known temperature while the tunnel was operating.

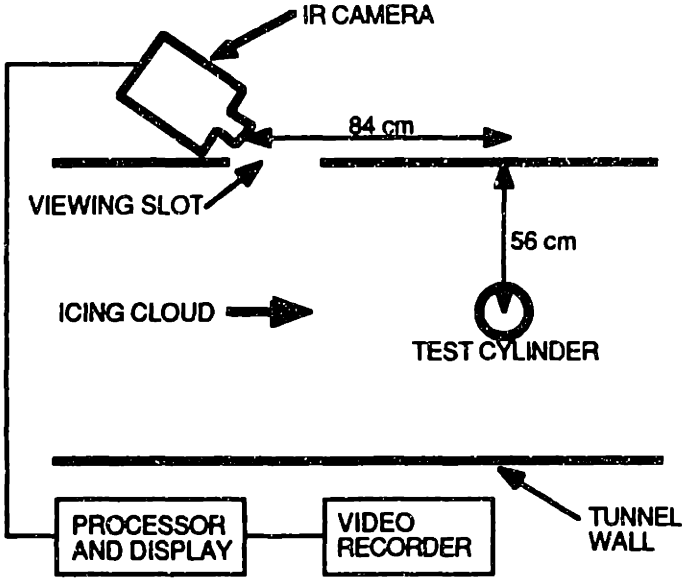

Fig. 4-5 Schematic diagram of the IR video system set-up in BFGT.

5. Experimental Observations and Discussion

The visible and infrared observations were largely recorded on videotapes. These data were later analyzed either by digitizing the video images using a computer, by taking photographs of the screen, or making tracings on the screen.

5.1. Ice Shapes

An example of a grazing angle view with a fan laser beam is shown in Figs. 5-1 and 5-2. In the Fig. 5-1, the test cylinder is partially illuminated to show the experimental set-up in the tunnel. In Fig. 5-2, the light in the wind tunnel is turned off to enhance the laser image. It should be noted that because the laser source is on top of the tunnel, the top half of the cylinder is better defined. Also, the bottom half is not illuminated initially, since the laser needs a continuous light path to travel to that part of the cylinder.

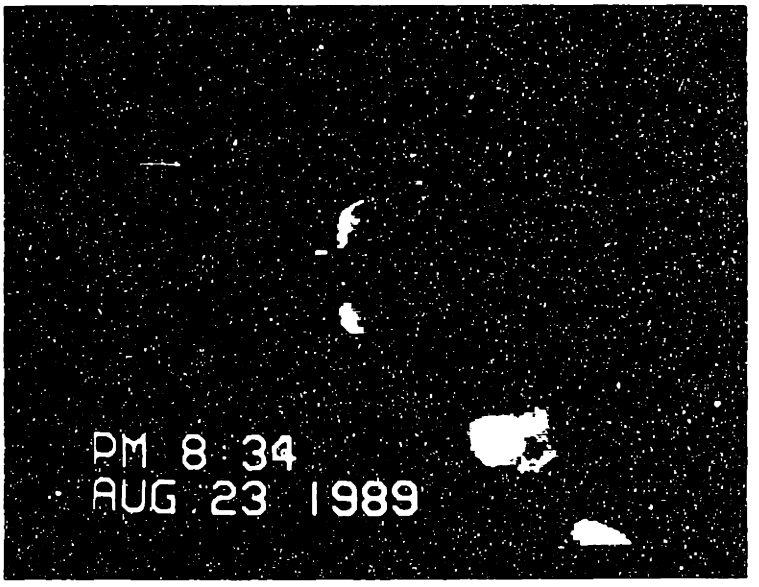

Fig. 5-1 Grazing view of the test cylinder with laser light sheet - partial illumination.

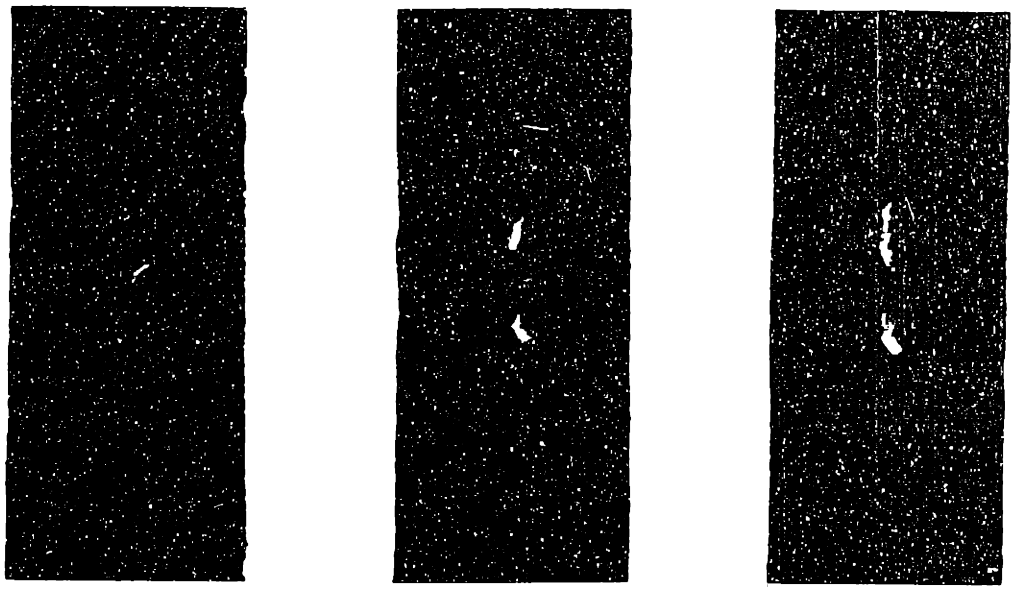

a. 40 secs b. 120 secs. c. 240 secs.

Fig. 5-2 Grazing view of the test cylinder with laser light sheet - with lights off.

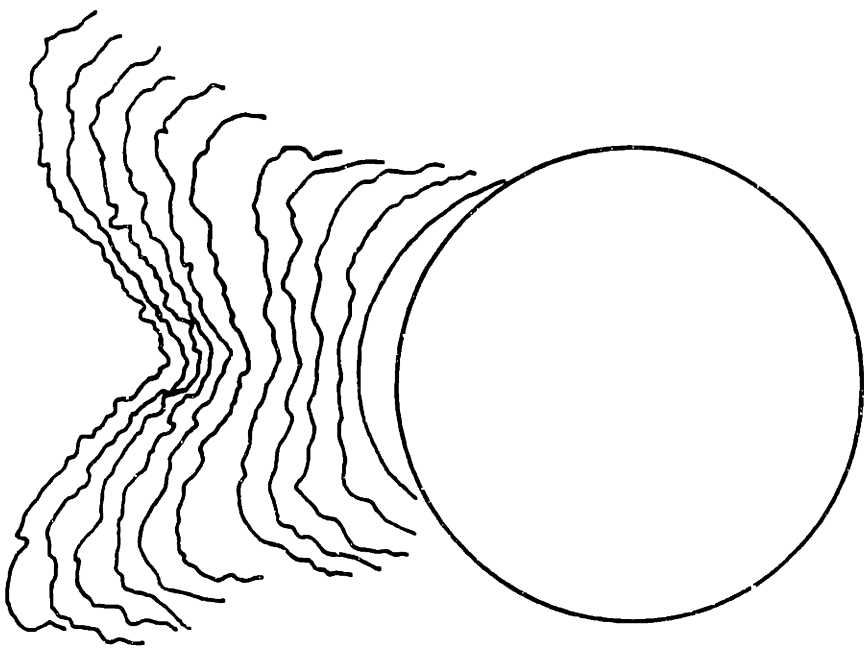

Fig. 5-3 Example of tracings of 4 minute ice accretion at 20 seconds intervals from BFGT tests (T = -17.8°C, V = 64.31 m/s, LWC = 0.8 g/m^3, MVD = 30 microns).

Ice shapes were recorded for a variety of icing parametric regions, mostly in the glaze ice regime. Because of the new laser light sheet set-up used in the BFGT, it was possible to obtain more detailed and accurate ice shape tracings (Fig. 5-3). These were used for comparisons with LEWICE. The results are discussed in Section 6.

5.2. Surface Roughness Regions

For glaze ice accretions, several regions with different surface roughness characteristics were observed during the detailed photographic analyses of the accreting ice surfaces. Although a total of five roughness zones were identified, rarely were more than three zones present on any particular ice accretion. The different zones are described briefly below.

5.2.1. Smooth Zone

Close to the stagnation point, the surface was observed to be uniformly wet with a thin film of water at warm temperatures. In this "smooth zone", the surface was smooth with no distinctively visible roughness. The extent of this zone was observed to vary with icing parameters, and is discussed in detail in Section 5.3.

5.2.2. Rough Zone

At some point downstream, there was a sudden transition to a significantly rougher zone, where there appeared to be insufficient water to maintain a uniform film, and the water tended to coalesce into the water beads first observed by Olsen and Walker.[10,11] In this "rough zone", the ice accretion rate was observed to be enhanced compared to the smooth zone. This is thought to be due to an increased heat transfer resulting from the greater surface roughness.

5.2.3. Horns

In certain glaze ice accretions, particularly at high liquid water contents, some of the roughness elements within all or part of rough zone were observed to grow into distinct protuberances. With higher collection efficiency and enhanced heat transfer, these protuberances tended to grow rapidly resulting in horned ice accretions. An example of such ice growth at a very warm temperature of -0.5°C is shown in Fig. 5-4.

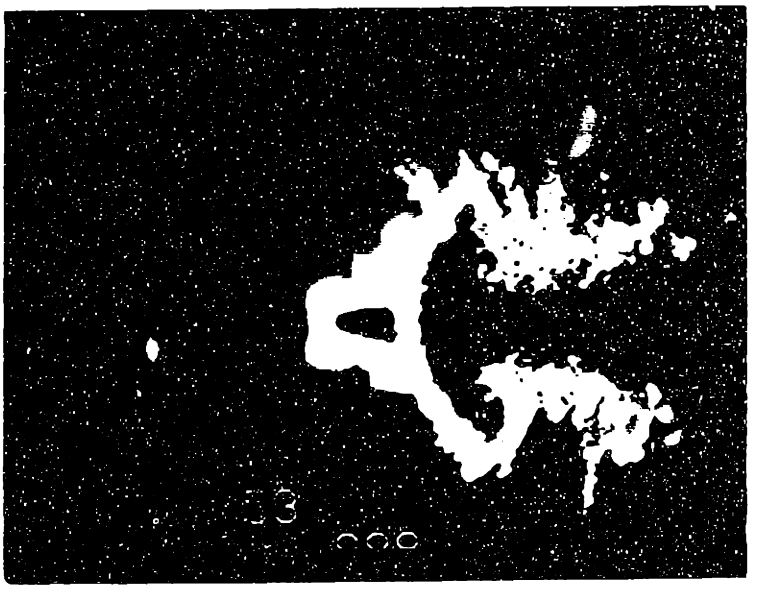

Fig. 5-4 Extreme example of horn elements for a warm glaze ice accretion (T = -0.5°C, V = 77.17 m/s, LWC = 1.0 g/m^3, MVD = 25 microns).

5.2.4. Runback Zone

At warm temperatures, a runback zone was observed aft of the rough zone, which was characterized by areas of ice interspersed with un-iced surface. This ice was observed to form during an initial transition period after cloud exposure. The surface water was

observed to initially runback and then stagnate at the point of flow separation, where this water slowly froze as rivulets or as large coalesced water cells. Once ice began to form in the upstream rough zone, no additional surface water was supplied to this zone, and the ice surface remained constant.

5.2.5. Rime Feathers

At cold temperatures, rime feathers were sometimes observed to grow in the region aft of the primary accretion. The feathers were dry ice accretion, which propagated in the local upstream direction.

5.3. Effect of Icing Cloud Parameters on the Smooth to Rough Transition

The angular position of the boundary between the smooth and rough zones has been observed as a function of time for cylinders. A typical example is shown in Fig. 5-5. The smooth/rough transition was observed to propagate with time towards the stagnation region for a wide variety of parametric conditions. The effect of icing cloud parameters on

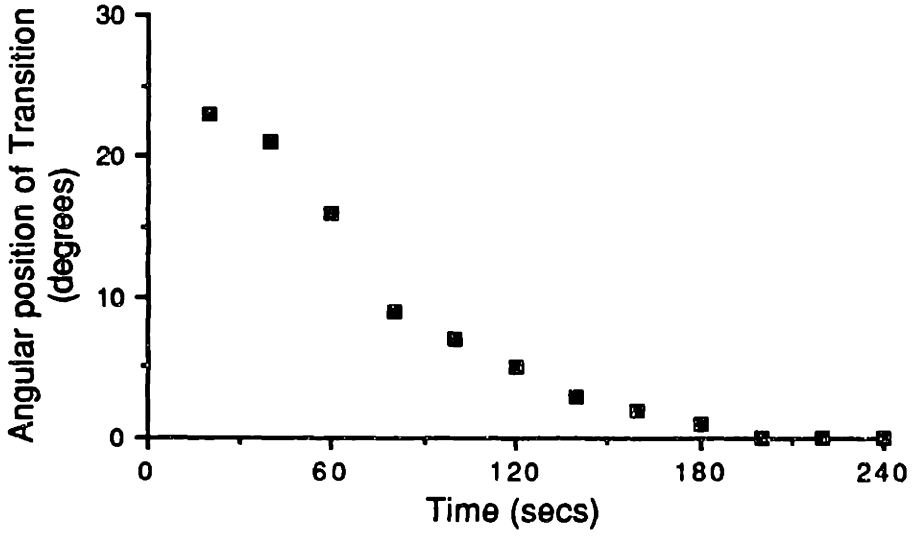

Fig. 5-5 Angular position versus time of smooth/rough transition location (T = -7°C, V = 64.31 m/s, LWC = 0.8 g/m^3, MVD = 12 microns).

the transition location have been studied in an attempt to identify the underlying physical mechanisms which cause the rough surface to develop.

The temperature, LWC, and freestream velocity effects on transition location were studied by holding all other parameters constant at nominal values. The nominal velocity was 77.17 m/s, the nominal LWC was 0.4 g/m^3 with MVD of 30 microns, and the nominal temperature was -4.5°C.

The effect of stream velocity is shown in Fig. 5-6. The higher velocity was observed to move the initial location of transition close to the stagnation . The effect of LWC is shown in Fig. 5-7. The higher LWC was seen to move the transition location faster towards the stagnation region. The effect of temperature is shown in Fig. 5-8. The warmer temperature indicates transition closer to the stagnation region. These observations imply that increasing Reynolds number causes the initial smooth/rough transition to move closer to the stagnation region, and increasing the flow of surface water causes the rate of movement of the transition point to increase.[17]

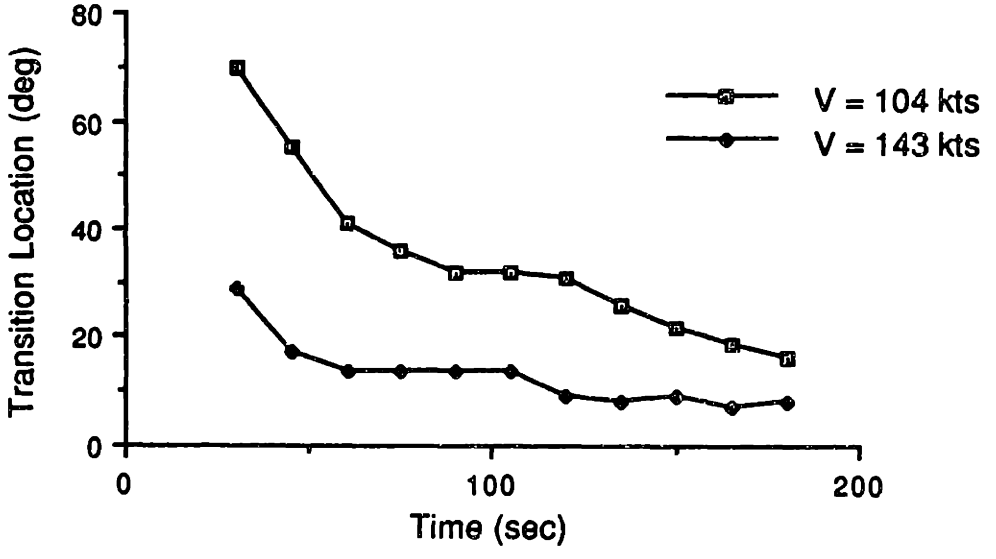

Fig. 5-6 The effect of freestream velocity on the transition location.

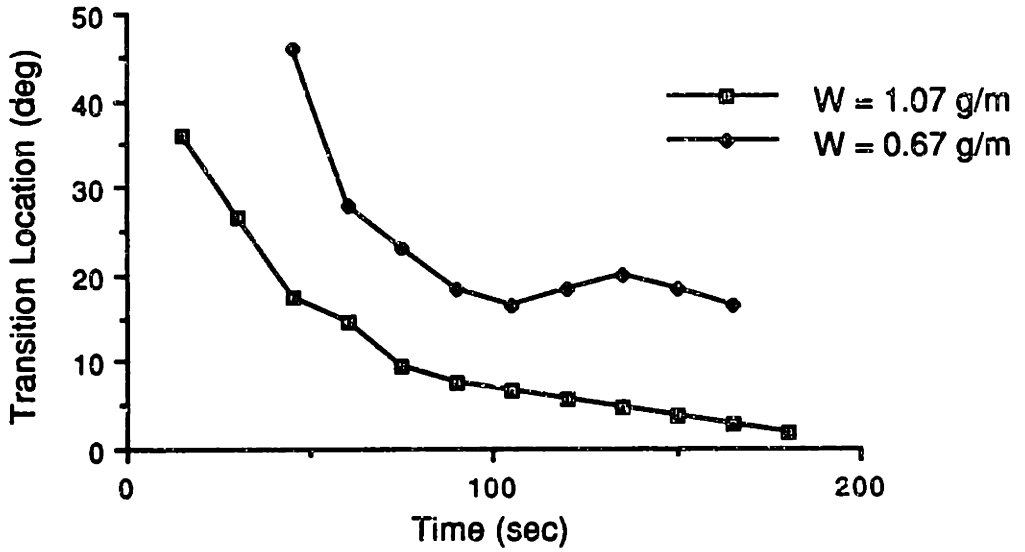

Fig. 5-7 The effect of LWC on the transition location.

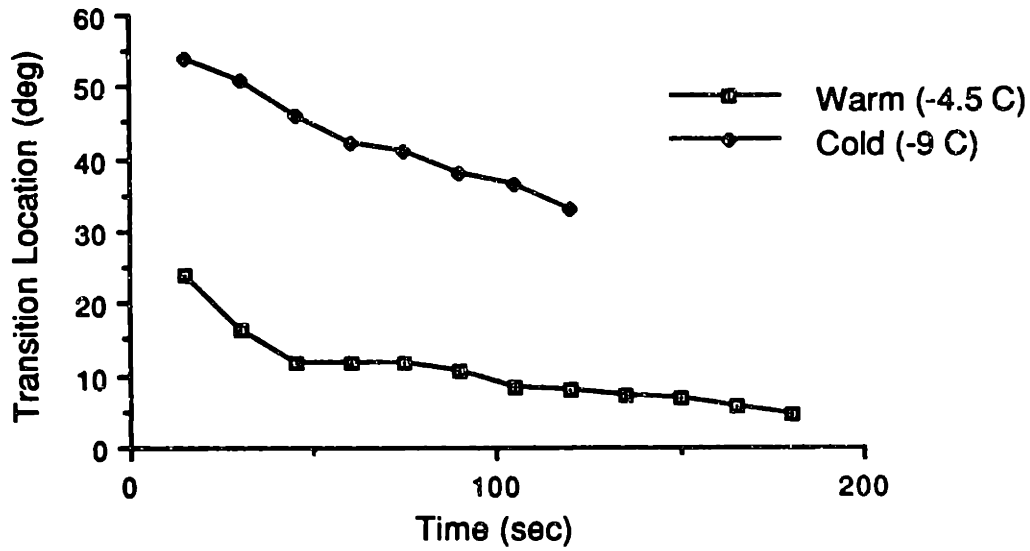

Fig. 5-8 The effect of temperature on the transition location.

5.4. Infrared Observations

Typical digitized thermal video images of a 2.5" cylinder during a 2 min. 15 sec. ice accretion in the BFGT through the IR camera are shown in Fig. 5-9. In this case the temperature was -4°C, the velocity was 77.17 m/s, and the liquid water content was 1.5 g/m^3. As a result of the way the IR camera was set-up, the cylinder was observed from above the horizontal and only the top of the cylinder was in view. In the images, the flow would be from below and a thermal profile corresponding to the mid-plane of the tunnel is shown on the right. (The set up is shown in Figure 4-5.)

Prior to exposure to the icing cloud, in Fig. 5-9a the cylinder was at a uniform temperature of -4°C, corresponding to the tunnel stagnation temperature. When the spray was turned on, the stagnation region quickly warmed to 0°C indicating wet growth. The wet region spread for approximately 75 seconds until it reached an equilibrium covering the foreword 50° of the cylinder. The equilibrium wet region can be seen in Fig. 5-9b. As horned growth began to appear in the wet region, the boundary of the wet region became irregular as exhibited in Fig. 5-9c. The enhanced heat transfer and the variation resulting from the rough surface and the horns can be seen in Fig. 5-9d, which was taken 10 seconds after the spray was shut off. At this time, a small wet region can still be observed in the stagnation area, due to the low heat transfer in that region.

The extent of the wet surface region was studied using the IR video system for a variety of conditions. It was found that both the surface roughness and horns were generated within the wet region. However, rime feathers were always observe in the dry region. The wet region was always centered around the stagnation line and its extent varied as a function of icing conditions, particularly temperature. The angular extent of the wet region is plotted as a function of temperature in Fig. 5-10. It was observed that the angular extent of wet region expanded with increasing temperature.

a. Before icing cloud exposure.

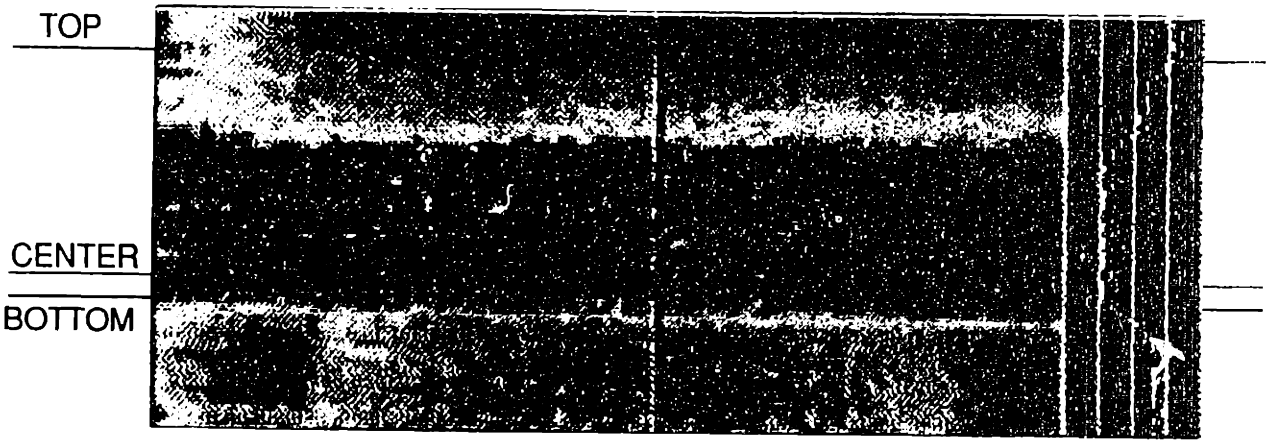

b. 75 seconds after exposure began.

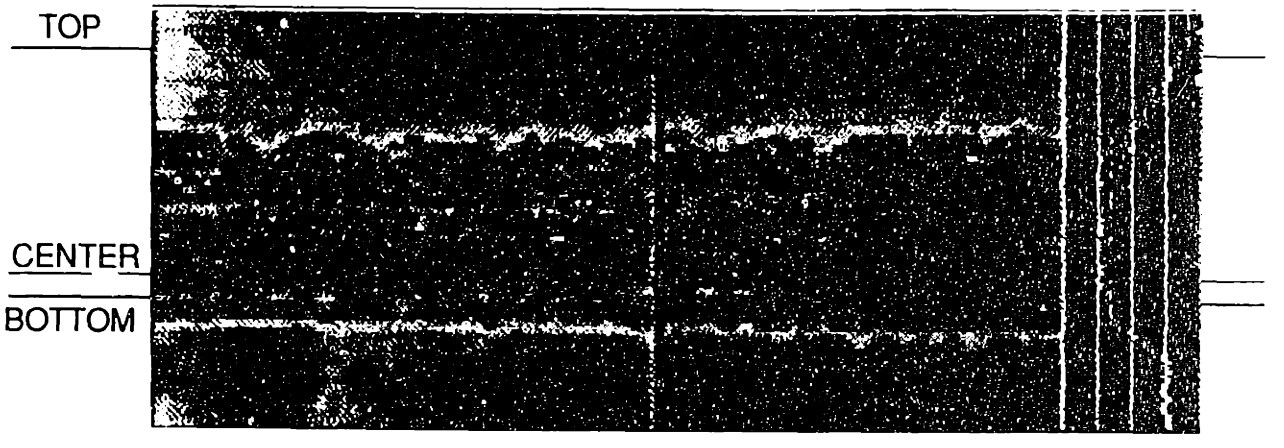

c. 135 seconds after exposure began.

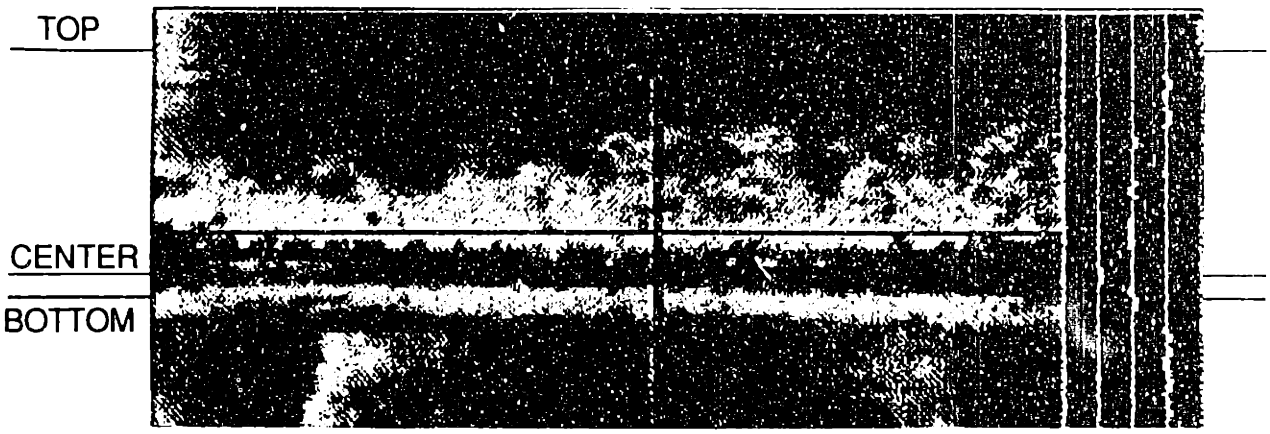

d. 10 seconds after exposure ended.

Fig. 5-9 Infrared thermographs of a 2.5" cylinder in BFGT, (T = -4°C, V = 77.17 m/s, LWC = 1.5 g/m3).

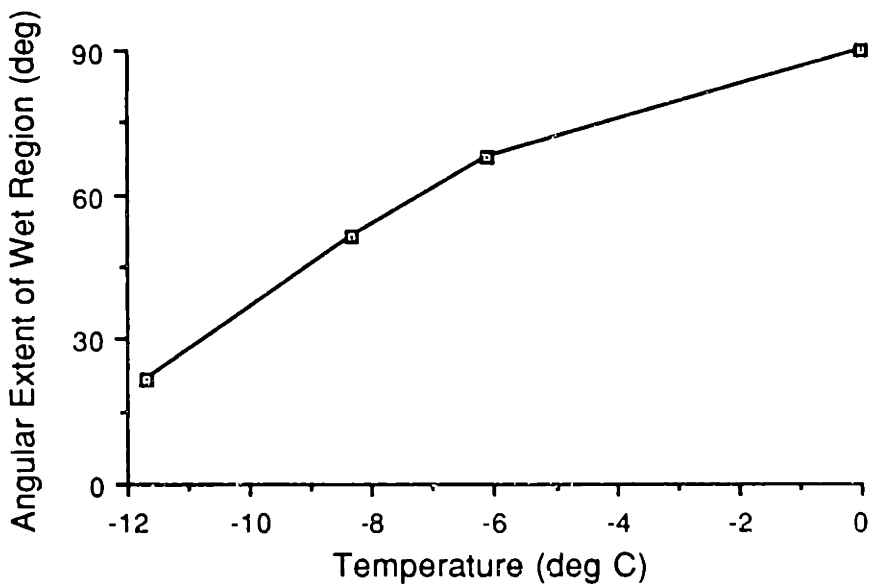

Fig. 5-10 Angular extent of wet region as a function of temperature for 2.5" cylinders in BFGT, (V = 77.17 m/s, LWC = 1.0 g/m^3).

6. Multi-Zone Model

The detailed photographic analyses of accreting ice surfaces revealed distinct zones with different surface roughness characteristics. Also, the boundary between the smooth and the rough zones were observed to propagate towards the stagnation region, and the effects of icing parameters on the transition location were analyzed. Based on these observations and analyses, a "Multi-Zone" model, in which the accreting ice surface is divided into two or more discrete zones with varying surface roughness and water behavior, was proposed.[18]

6.1. Model Description

In contrast to the conventional techniques which assume uniform roughness over the entire ice accretion, the "Multi-Zone" model is divided into two or more discrete zones with varying surface roughness and water behavior in order to be consistent with experimental observations.

In the simplest version of the model, the surface is divided into two zones, the "smooth" zone and the "rough" zone. In the "smooth" zone, corresponding to the smooth region centered about the stagnation line, the surface is uniformly wet, with thin water film runback. The heat transfer is that for laminar boundary layer and a Messinger type runback model used in the original LEWICE appears valid.[9]

In the "rough" zone, surface tension effects are important and the characteristic water beads or roughness elements appear. Here, the heat transfer is enhanced due to increased roughness and the experimental results have indicated no water runback in this region for some cases.[4,10,11,19] Without runback, the freezing fraction can be assumed to be unity.

6.2. Surface Roughness Transition Model

Based on the experimental observation of smooth to rough transition location, it is hypothesized that the smooth/rough transition location can be assumed to coincide with the laminar/turbulent boundary layer transition for the purpose of ice accretion prediction. It is also thought that the laminar/turbulent transition follows the smooth/rough transition as it propagates toward the stagnation region.

6.2.1. Initial Smooth/Rough Transition and Boundary Layer Transition

Observations that the initial surface roughness transition from smooth to rough depends on Reynolds number, as seen in Fig. 5-6, indicate that, in certain conditions, the initial transition in surface roughness is controlled by boundary layer transition. In these cases, the laminar/turbulent boundary layer transition point will also be the initial smooth/rough transition point.

6.2.2. Bead Formation and Propagation of the Transition Location

In the laminar region, the heat transfer is low enough that not all of the impinging water mass is frozen and the surface is coated by a uniform water film. However, the enhanced heat transfer in the turbulent region can cause sufficient freezing to partially dry the surface and cause bead formation, which results in the increased roughness observed in the rough region. The observations that higher surface water flow causes the rate of movement of the transition to increase (Fig. 5-7), support this hypothesis.

The influence of surface water flow on the smooth/rough transition location also indicates that dynamic effects are important. It is thought that the dynamic effects are caused by bead formation at the interface between the smooth and rough surface zones as

shown in Fig. 6-1. The initial smooth/rough transition occurs because of the boundary layer transition as discussed above. Then, a bead, which is formed at the interface, causes the boundary layer to transition to turbulent upstream of the bead, enhancing the heat transfer in the region where the bead is formed. With the enhanced heat transfer, the bead freezes, forming rough ice, and as the surface dries, beads begin to form further upstream and the transition point will propagate towards the stagnation region as observed experimentally. By increasing the surface water flux, the rate of formation and growth of the interfacial beads is increased. This causes the observed increase in upstream propagation of the transition point with increasing surface water flux.

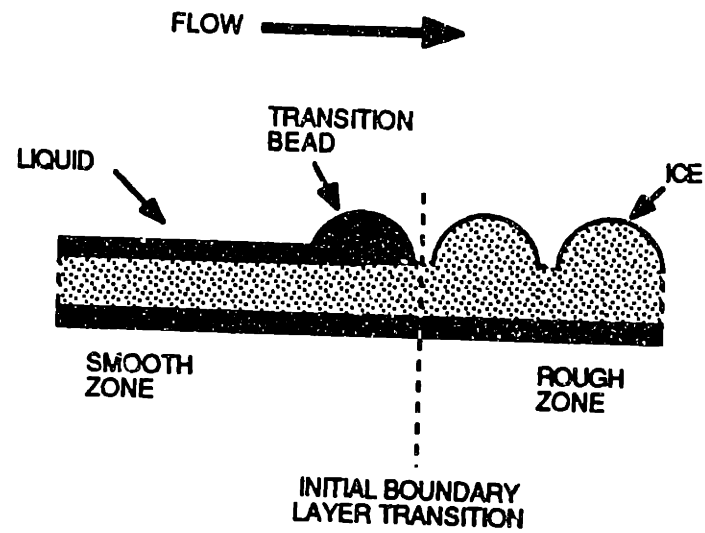

Fig. 6-1 Schematic representation of bead formation at the smooth to rough transition.

6.3. Initial Implementation in LEWICE

Based on the hypothesis that the smooth/rough transition location coincides with the laminar/turbulent boundary layer transition, a simple, more physically realistic, Multi-Zone model was implemented in the LEWICE code. Initially, a simple two-zone version of the Multi-Zone model was implemented through boundary layer transition in order to evaluate

the effectiveness of the model. In this implementation, the smooth and rough zones are considered to coincide with the regions of laminar and turbulent boundary layer, which are treated separately when calculating heat transfer in LEWICE.

For the first time step, two different roughness are used for the laminar and the turbulent regions. As explained previously, the roughness element height is used for two different purposes in the two regions in LEWICE. By using two roughness element sizes, one for the laminar region and the other for the turbulent region, it is possible to control the transition location and the turbulent heat transfer independently. The laminar roughness is then used to determine the laminar to turbulent boundary layer transition location. The turbulent roughness is used to calculate the heat transfer coefficient in the turbulent region. This method more closely emulates the physical situation where two different roughness element heights have been observed in the smooth and rough zones. In the laminar region, a roughness height k_l, corresponds to the roughness of the uniform water film. In the turbulent region, the roughness height k_t corresponds to the roughness size observed in the rough zone. This method is valid only for the first time step, where the transition location is determined mainly from the boundary layer transition around the accreting body and the dynamic effects of surface water are negligible.

In subsequent time steps, the boundary layer transition point is made to propagate towards the stagnation line in a manner consistent with experimental observations of the smooth/rough transition. For this preliminary implementation, transition locations as a function of time are input to the code from experimental data. The roughness element height k_t for the turbulent region still needs to be specified. For some cases, however, the experimental results have indicated that freezing fraction is unity in this region. For these cases, the ice shape is not dependent on the roughness element height that user chooses, as long as k_t is large enough to ensure that there is enough heat transfer to remove all the latent heat. This is analyzed more in detail in Chapter 7.

6.4. Deterministic Smooth/Rough Transition

In the preliminary implementation of the Multi-Zone model, the experimentally observed smooth/rough transition locations were input as the laminar/turbulent transition location, as described in the previous section. The next step in the implementation of the Multi-Zone model is to implement a method for calculating the transition location based on the input parameters. One such implementation utilizes the observed formation of beads described in Section 6.2.2.

To better understand the relationship between the surface water mass flux and the size of the bead, the thickness of the surface water/bead was estimated using the experimentally observed locations of smooth/rough transition (Fig. 6-2) and analytically calculated surface water flux for an example case with velocity of 64.31 m/s and LWC of 0.8 g/m^3. The thickness of the water film was first estimated from mass conservation:

$$\text{Thickness} = \frac{\dot{m}\,\Delta t}{\rho x} \qquad [6\text{-}1]$$

where m is the mass flux calculated by LEWICE, Δt is the time step size considered, ρ is the density of water, and x is the distance covered by the mass. For each of the 20 second intervals, the thickness of the water film was calculated. It was found that, although there was some variation, the average was about 2 mm.

Based on these calculations, a method for deterministically calculating the smooth to rough transition location was proposed. For this purpose, the water film thickness has some defined thickness. From the mass flux calculated by LEWICE, the transition location can be calculated by:

$$x = \frac{\dot{m}\,\Delta t}{(\text{thickness})\,\rho} \qquad [6\text{-}2]$$

where x is the distance covered by mass, Δt is the time step used to run LEWICE, m is the mass flux calculated by LEWICE. The result of this calculation is shown in Fig. 6-2, where the thickness was assumed to be 2 mm. It was found that for this particular case, the transition location can be calculated well.

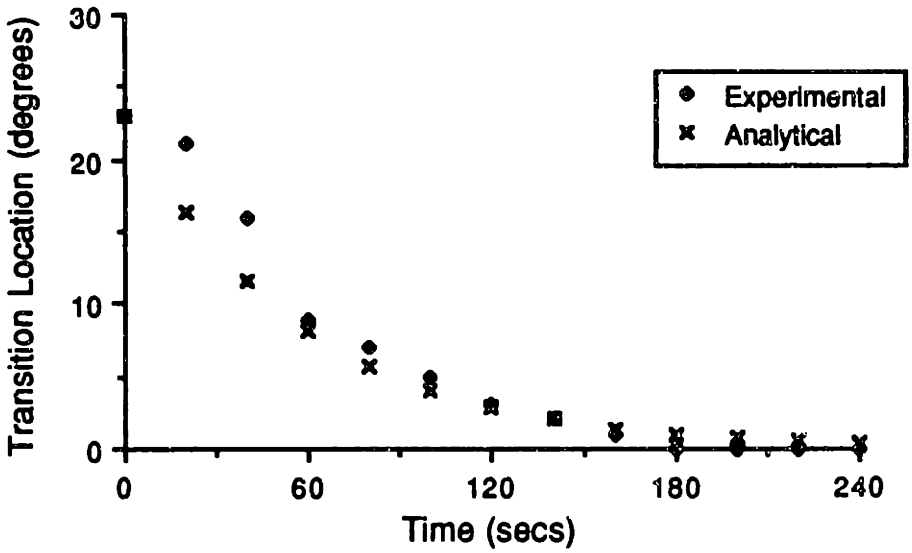

Fig. 6-2 Deterministic transition location versus time (T = -7°C, V = 64.31 m/s, LWC = 0.8 g/m^3, MVD = 12 microns).

The deterministic smooth/rough transition model was implemented in LEWICE for the case shown in Fig. 6-2. For this implementation, the initial location of laminar/turbulent transition was input based on the experimental observation of smooth/rough transition location. Then, the transition location was calculated for the subsequent time steps based on the algorithm discussed above. The result is presented in Chapter 7.

7. Ice Shape Comparisons

In order to verify the effectiveness of the Multi-Zone model, ice accretion predictions calculated by LEWICE was compared to the experimental data of the ice shapes obtained during experiments conducted in the icing wind tunnels

7.1. Example 1

The first ice shape comparison example is shown in Fig. 7-1, for a 4 minute ice accretion at 20 second intervals on a 1 inch cylinder. The icing cloud condition was -7°C, LWC of 0.8 g/m^3, and MVD of 12 microns , and the velocity was 64.31 m/s. The experimentally observed smooth/rough transition locations are shown in Fig. 7-2. The surface roughness elements were observed to be on the order of 1 mm in the rough zone.

The original LEWICE was run using the equivalent sand grain surface roughness size of 0.04174 mm, calculated using the Ruff correlation For this case, the ice shapes indicate no transitioned to a rougher zone with increased ice accretion. Here, the boundary layer never transition to turbulent and the heat transfer calculated was for that of the laminar boundary layer. Therefore, the original LEWICE is clearly seen to underpredict the ice accretion for this case.

For the first Multi-Zone run, the experimentally observed smooth/rough transition location shown in Fig. 6-2 was used as the laminar/turbulent transition location input. The value of the roughness input parameter used in the turbulent region for this case was 1.0 mm, based on the experimental observation of the surface roughness. Both the smooth and rough ice zones were predicted using the Multi-Zone model, and there is a good correlation between the experimentally observed ice accretion and predicted ice accretion.

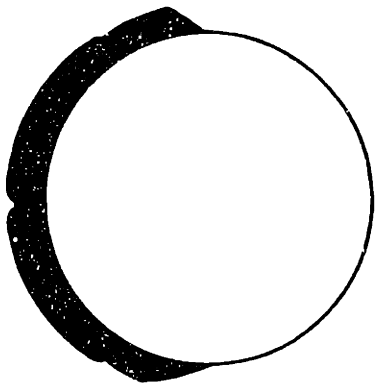

a. Original LEWICE prediction.

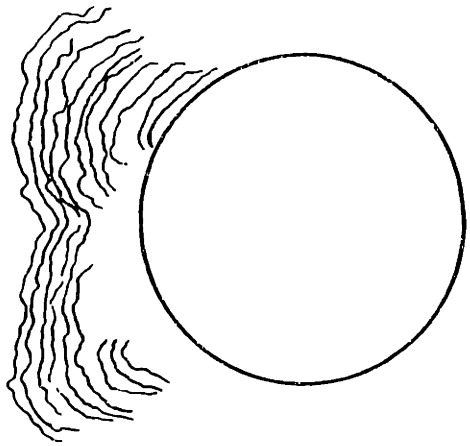

b. Experimentally observed ice shape.

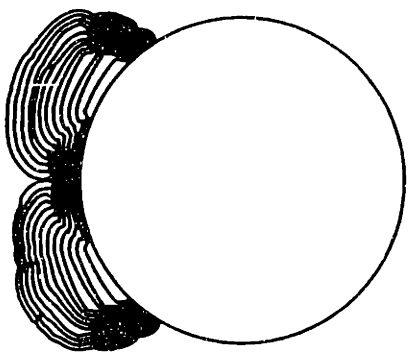

c. Modified LEWICE prediction with experimental transition input.

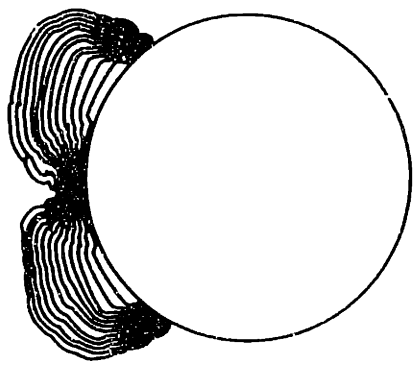

d. Modified LEWICE prediction with deterministic transition location.

Fig. 7-1 Comparison of experimental and predicted ice shapes for a 1 inch cylinder, (T = -7°C, V = 64.31 m/s, LWC = 0.8 g/m^3, MVD = 12 microns).

The Multi-Zone model with deterministic transition location algorithm was also run. For this case, the initial location of laminar/turbulent transition was input from the experimentally observed location of smooth/rough transition location. For subsequent time steps, the transition location was calculated using the algorithm discussed in Sec. 6.4 and is presented in Fig. 6-2. The value of the roughness input parameter used in the turbulent region for this case was 1.0 mm. This resulted in a result similar to the one with the Multi-Zone run with, indicating that glaze ice can bemore accurately predicted with this algorithm.

7.2. Example 2

The second ice shape comparison example is shown in Fig. 7-2, for a 150 second ice accretion on a 1" cylinder. The icing cloud condition was -5.6°C, LWC of 1.0 g/m^3, and MVD of 30 microns, and velocity was 65.17 m/s. The experimentally observed smooth/rough transition locations used for the Multi-Zone runs are shown in Fig. 7-3.

The accretion predicted by the original LEWICE is shown in Fig. 7-2a. The equivalent sand grain roughness used was 0.0253 mm, as calculated using the Ruff correlation. The ice accretion is under predicted for this case.

The experimentally observed smooth/rough transition locations, at times 45, 105, and 150 seconds, were used as the laminar/turbulent transition location input to the LEWICE code with Multi-Zone model implementation. The value of roughness size used in the turbulent region for this case was 1.0 mm, based on the experimental observations of the surface roughness. It should be noted that both the original and modified LEWICE codes were run for times 45, 105, and 150 seconds, while the tracings from the experimental results represents ice accretions at 30, 90, and 150 secs. The overall ice shape is well predicted for this case, with smooth zone around the stagnation region and rough zone with increased ice accretion aft of the smooth region.

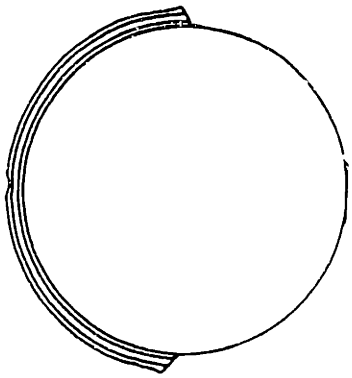

a. Original LEWICE prediction at 45, 105, and 150 seconds.

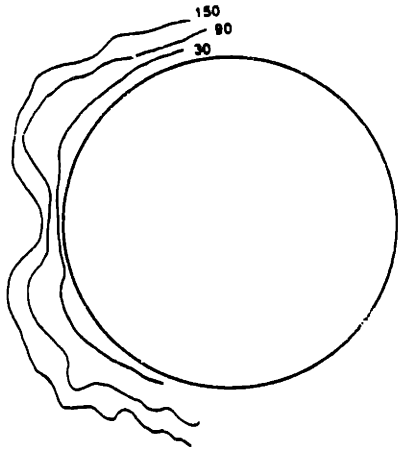

b. Experimentally observed ice shape at 30, 90, and 150 seconds.

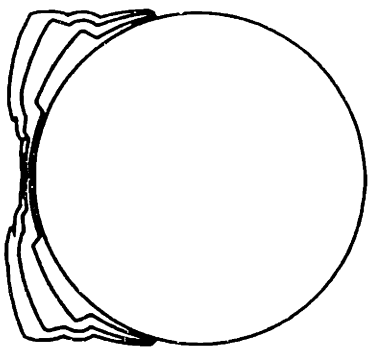

c. Modified LEWICE prediction at 45, 105, 150 seconds.

Fig. 7-2 Comparison of experimental and predicted ice shapes for a 1 " cylinder, (T = -5.6°C, V = 65.17 m/s, LWC = 1.0 g/m3, MVD = 30 microns).

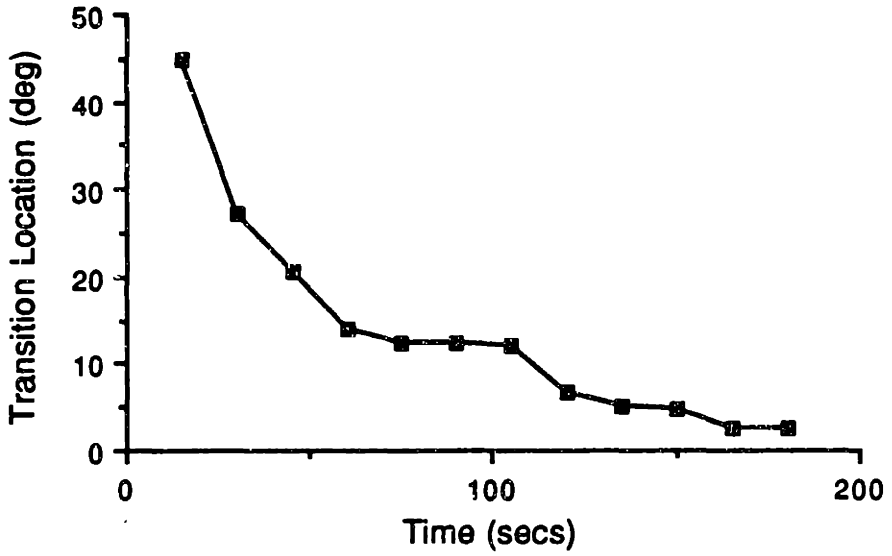

Fig. 7-3 Angular position versus time of smooth/rough transition location for the example shown in Fig. 7-2.

7.3. Roughness Element Sizes

One of the problems found while running the original LEWICE code was the discrepancy between the physical roughness element height observed in the experiments and the value of the roughness eler ient height required for the LEWICE code. It was found that for the icing cloud conditions and cylinders used in the experiments, the Ruff correlation roughness height was at least an order of magnitude smaller than the experimentally observed roughness height. The roughness heights calculated using the Ruff correlation were not physically reasonable, on the order of a few hundredth of a millimeter. The Ruff correlation was derived based on a limited data base of NACA 0012 airfoils. The valid range of parameters , velocity, LWC, temperature, and chord length, for which the correlation is based, should be investigated.

8. Conclusions

The investigation of the effects of surface roughness and heat transfer on ice accretion modeling has resulted in the following conclusions:

1. The use of roughness element height in LEWICE ice accretion prediction code has been investigated. It was found that the roughness is used to determine the location of the laminar to turbulent boundary layer transition and to calculate the heat transfer in the turbulent boundary layer. The heat transfer in the laminar region is independent of the roughness element height.

2. Increasing the roughness height in the laminar boundary layer was observed to move the laminar to turbulent boundary layer transition location closer to the stagnation region. Increasing the roughness in the turbulent boundary layer increased the magnitude of the turbulent heat transfer coefficient.

3. The heat transfer predicted by LEWICE was compared with a set of experimental heat transfer coefficient data on roughened cylinders. It was found that using a physical value of roughness element size in the turbuient region, a more accurate technique for determining the laminar/turbulent transition location, and viscous flow field, the heat transfer could be predicted accurately.

4. A fan laser technique was used to obtain high resolution profiles of ice accretions and accurate locations of smooth/rough transition. This technique significantly improved the facility and accuracy of the photographic observation.

5. Glaze ice accretions were observed to have distinct zones of roughness and surface water behavior. Five such zones were observed. They were: a smooth zone in the stagnation region with uniform water film runback; a rough zone where increased

heat transfer caused dry ice accretion and water beads were observed; a horn zone which were observed to emerge out of the rough zones with large roughness elements; a runback zone, where surface water froze as rivulets; and a zone where rime feathers grew.

6. The transition location between the smooth zone near stagnation region and rough zone was observed to propagate towards stagnation region with time.

7. The effects of icing cloud parameters, such as LWC, temperature, and velocity, were investigated. It was found that increasing surface water increased the rate of propagation towards stagnation region, while increasing the Reynolds number moved the initial smooth/rough transition closer to the stagnation region.

8. Infrared video observations were made of accreting ice surfaces. This technique was used to observe the extent of wet region during ice accretion. It also revealed the difference in heat transfer for different roughness zones.

9. Based on the experimental results and a hypothesis that the laminar/turbulent boundary layer transition location coincides with the observed smooth/rough transition location, a simple modification to the current ice accretion modeling technique, implementation of the "Multi-Zone" model, was proposed.

10. An initial two-zone version of the "Multi-Zone" model was implemented in the LEWICE code. For this implementation, experimentally observed smooth/rough transition location was used as an input. The experimental observations of the glaze ice accretion were used to verify the concept of the Multi-Zone model. The Multi-Zone model significantly improved the prediction of the glaze ice accretion.

11. A deterministic smooth/rough and boundary layer transition location model, based on experimental observations, was proposed. In the limited data set examined, the

deterministic model appears to give good results if the boundary layer transition location on the initially forming ice surface can be accurately determined.

References

1. Kirby, M., *An Experimental and Theoretical Study of the Ice Accretion Process during Artificial and Natural Icing Conditions*, MS Thesis, Department of Aeronautics and Astronautics, Massachusetts Institute of Technology, May, 1986.

2. MacArthur, C.D., "Numerical Simulation of Airfoil Ice Accretion,", AIAA Paper 83-0112, January, 1983.

3. Ruff, G.A., "Development of an Analytical Ice Accretion Prediction Method (LEWICE)", Sverdrup Technology, Inc., LeRC Group Progress Report, February 1986.

4. Hansman, R.J., and Turnock, S., "Investigation of Surface Water Behavior During Glaze Ice Accretion", AIAA Paper 88-0115, Jan. 1988.

5. Hess, J.L. and Smith, A.M.O., "Calculation of Potential Flow about Arbitrary Bodies." Progress in Aeronautical Sciences, 8:1-138, (D. Kuchemann, editor). Elmsford, New York, Pergmon Press, 1967.

6. LEWICE Users Manual, 1988.

7. Gear, C.W., "The Automatic Integration of Ordinary Differential Equation," Comm. ACM 14, 1971, pp. 176-179.

8. Gear, C.W., "DIFSUB for Solutions of Ordinary Differential Equations," Comm. ACM 14, 1971, pp. 185-190.

9. Messinger, B.L., "Equilibrium Temperature of an Unheated Icing Surface as a Function of Airspeed," *Journal of the Aeronautical Sciences*, Jan. 1953, pp. 24-42.

10. Olsen, W., and Walker, E., "Close up Motion Pictures of the Icing Process," NASA LeRC Film, 1983.

11. Olsen, W.A., and Walker, E., "Experimental Evidence for Modifying the Current Physical Model for Ice Accretion on Aircraft Structures," NAS TM 87184, 1987.

12. von Doenhoff, A.E., and Horton, E.A., "A Low Speed Experimental Investigation of the Effect of Sandpaper Type of Roughness on Boundary Layer Transition," NACA TN 3858, 1956.

13. Riley, J., Safety Analysis Branch, Federal Aviation Administration Technical Center, Atlantic City, NJ.

14. White, M., Viscous Fluid Flow, McGraw-Hill, Inc., 1974.

15. Achenbach, E., "The Effect of Surface Roughness on the Heat Transfer from a Circular Cylinder to the Cross Flow of Air", *International Journal of Heat and Mass Transfer*, Vol. 20, 1977, pp. 359-369.

16. Zukauskas, A., and Ziugzda, J., Heat Transfer of a Cylinder in Cross Flow, Hemisphere Publishing Corporation, 1985.

17. Hansman, R.J., Yamaguchi, K., Berkowitz, B., and Potapczuk, M., "Modeling of Surface Roughness Effects on Glaze Ice Accretion", AIAA Paper 89-0734, Jan. 1989.

18. Yamaguchi, K., Hansman, R.J., "Heat Transfer on Accreting Ice Surfaces", AIAA Paper 90-0200, Jan. 1990.

19. Hansman, R.J., and Turnock, S., "Investigation of Microphysical Factors Which Influence Surface Roughness During Glaze Ice Accretion", *Proc. 4th Intl. Workshop on the Atmospheric Icing of Structures*, Sept. 1988.

20. Kays, W.M., and Crawford, M.E., Convective Heat and Mass Transfer, Second Edition, McGraw-Hill Book Company, 1980.

Appendix A: Mass and Energy Balance Equations*

A.1. Mass Balance

A schematic diagram of a control volume with mass flux is shown in Fig. A-1. The mass balance for a control volume can be expressed as a sum of incoming mass flux minus the sum of outgoing mass flux:

$$\dot{m}_c+\dot{m}_{r_{in}}-\dot{m}_e-\dot{m}_{r_{out}}=\dot{m}_i \qquad [A\text{-}1]$$

where m_c is the impinging water mass flux, m_{rin} is the water flow into the control volume, m_e is the evaporation, m_{rout} is the water flow out of the control volume, and m_i is the ice accumulation.

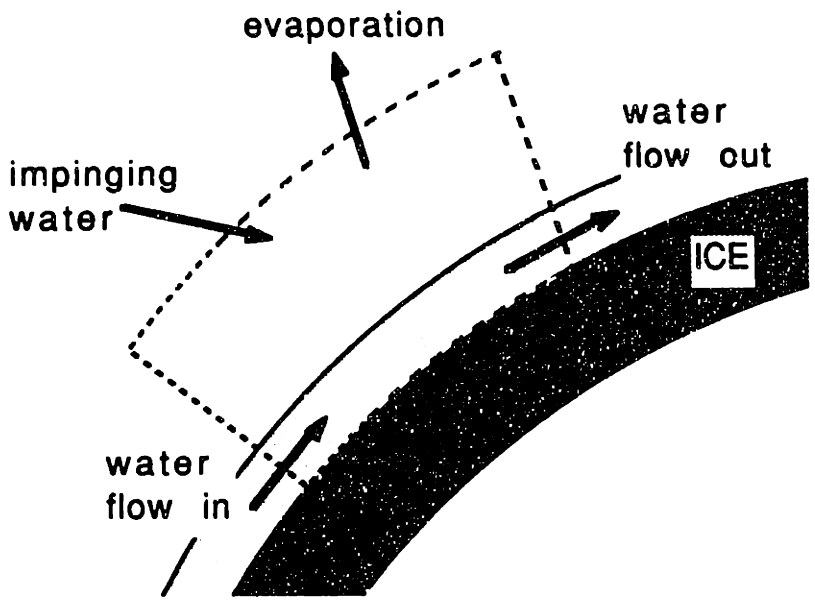

Fig. A-1 Schematic representation of a control volume with mass flux.

Then the freezing fraction , f, is:

---

* These equations were taken from the LEWICE Users Manual [Ref. 7].

$$f = \frac{\dot{m}_i}{\dot{m}_c + \dot{m}_{r_{in}}} \qquad [A\text{-}2]$$

and the water flow out of the control volume can be calculated:

$$\dot{m}_{r_{out}} = (1 - f)\,(\dot{m}_c + \dot{m}_{r_{in}}) - \dot{m}_e \qquad [A\text{-}3]$$

A.2. Energy Balance

The energy balance for a control volume is shown in Fig. A-2. The components of the energy balance are:

(1)	Impinging Water	$\dot{m}_c\, i_{w,T}$
(2)	Evaporation	$\dot{m}_e\, i_{v,sur}$
(3)	Internal energy of water flow out	$\dot{m}_{r_{out}}\, i_{w,sur}$
(4)	Internal energy of water flow in	$\dot{m}_{r_{in}}\, i_{w,sur(i-1)}$
(5)	Conduction	$q_k\, \Delta s$
(6)	Convection	$q_c\, \Delta s$
(7)	Latent heat released by freezing water	$\dot{m}_i\, i_{i,sur}$

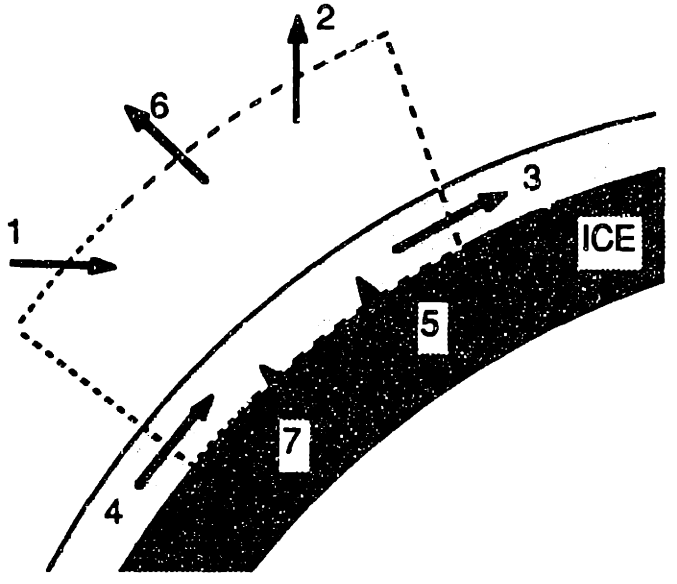

Fig. A-2 Schematic description of heat balance for a control volume.

The general form of the energy equation is:

$$\dot{m}_c\, i_{w,T} + \dot{m}_{r_{in}}\, i_{w,sur(i-1)} = \dot{m}_e\, i_{v,sur} + \dot{m}_j\, i_{j,sur} + q_c\, \Delta s + q_k\, \Delta s + \dot{m}_{r_{ex}}\, i_{w,sur} \quad [A\text{-}4]$$

(1) + (4) = (2) + (3) + (5) + (6) + (7)

Appendix B: List of LEWICE Input and Output Parameters

B.1. Inputs

The inputs to the LEWICE code consist of information on icing conditions, geometries of the bodies involved, and various other parameters necessary for calculations of flow field, impingement behavior, and ice accretion process. Some of these parameters are easily defined by the icing process the user is attempting to simulate, while others need to be calculated based on guidelines and equations suggested by the LEWICE Users Manual.

Table B-1 lists all the physical input parameters to LEWICE. These parameters define the accreting body shape and the icing cloud conditions. For each of the parameters, the section of the code in which it is used is listed as "Flow" for flow filed calculation section, "Trajectory" for trajectory and impingement calculation section, and "Ice " for thermodynamic and ice shape calculation section.

Table B-2 lists the numerical parameters which are needed throughout the program. The majority of them are used in the flow field calculation section, since this section was originally written for other purposes and has capabilities that are not necessary for ice prediction. Some of the parameters used in the trajectory calculation section defines the accuracy criterion. Depending on the values used, the computation time can vary from less than an hour to few hours per time step.

The interactive inputs are listed in Table B-3. These are the inputs required while the program is running. In order to run in the batch mode, the responses to these prompts must be included in a separate input file. There are other inputs required for special cases, such as when multiple stagnation points have been calculated. The responses required for these can vary and are explained in the LEWICE Users Manual.

Table B-1 Physical input parameters for LEWICE code

Parameters	Usage	Explanation
CHORD	Trajectory	Airfoil chord, [m]
CLT	Flow	Value of angle of attack or lift coefficient (depends on INCLT)
DPD	Trajectory	Droplet sizes in the distribution
DPMM	Ice	Mass median droplet diameter, [microns]
FLWC	Trajectory	Fraction LWC of each droplet size in the distribution
G	Trajectory	Acceleration of gravity, [m/s^2]
LWC	Ice	Liquid water content, [g/m^3]
PAMB	Ice	Static pressure, [Pa]
RH	Ice	Percent relative humidity
TAMB	Ice	Static temperature, [°K]
VINF	Ice	Free-stream velocity, [m/s]
X, Y	Flow	Coordinates defining the accreting body
XKINIT	Ice	Initial value of the equivalent sand grain roughness of the icing surface, [m]

Table B-2 Numerical input parameters for LEWICE code.

Parameter	Usage	Default Value	Explanation
CCL	Flow		The value for the reference length (chord)
CFP	Trajectory		Cunningham correction factor
DSHIFT	Trajectory	.002	X-distance to shift coordinates after the potential flow calculation to avoid discretization errors
GEPS	Trajectory	.0005	Convergence criteria for the integration method of Gear
ICHORD	Flow	0	Flag indicating how reference length used in calculating C_l is input (0 = set to 1.0, 1 = input as CCL)
ICOMB	Flow	NO	Combination solution flag

IFILL	Flow	1	Parabolic integration flag (0 = results of parabolic integration not printed, 1 = the results are printed)
IFIRST	Flow	3	First-order terms flag (0 = no first-order term, 1 = first derivative term, 2 = curvature term, 3 = both first-order terms)
ILIFT	Flow	1	Lift control flag (0 = not lifting body, 1 = lifting body)
INCLT	Flow	0	α or C_l flag (0 = α is input as CLT, 1 = total lift coefficient is input as CLT)
IND	Flow	1	The individual solution flag (0 = no edge velocity for each body calculated, 1 = edge velocity for each velocity calculated)
INO	Flow		Number of data points per line
IPARA	Flow	1	Element geometry flag (0 = Linear elements, 1 = parabolic elements)
IPVOR	Flow	1	Vorticity distribution flag (0 = use constant vorticity between body elements, 1 = use variable vorticity distribution)
ISECND	Flow	3	Second-order terms flag (0 = no second-order term, 1 = second derivative term, 2 = curvature squared term, 3 = both second-order terms)
ISOL	Flow	0	Matrix solution method control flag (0 = use routine SOLVIT, 1 = use routine QUASI, 2 = use routine MIS1)
ISTAT	Flow		Last line flag (0 = not last line, 1 = last line)
ITYPE	Flow		X or Y coordinate flag (3 = X, 4 = Y)
LCMB	Trajectory	0	Combination correction flag (0 = use S24Y, 1 = use COMBIN-2D)
LCMP	Trajectory	0	Compressibility correction flag (0 = no correction, 1 = correct velocity values)
LEQM	Trajectory	1	Particle initial condition flag (0 = initial particle velocity is input, 1 = initial particle velocity is equal to the flow at initial location)
LSYM	Trajectory	0	Symmetric flow field flag (0 = unsymmetric flow field, 1 = symmetric flow field)
LXOR	Trajectory	1	X-coordinate particle release flag (0 = particle released from XORC, 1 = program determines the initial x location)
LYOR	Trajectory	1	Y-coordinate particle release flag (0 = particle released from YORC, 1 = program determines the initial y location)
NEQ	Trajectory	4	Number of equations to be solved to determine the particle trajectories
NPL	Trajectory	15	Number of particle trajectories to be computed to define the y_0 vs. s curve

NSEAR	Trajectory	50	Maximum number of trajectories allowed to be calculated in the search for the upper and lower impingement limits
NSI	Trajectory	1	Number of droplet size increments used to characterize the cloud droplet distribution
PIT	Trajectory	0.0	Initial angle of the particle flight reference line [deg]
PITDOT	Trajectory	0.0	Time derivative of the particle flight reference line [deg/sec]
PRATK	Trajectory	0.0	Initial value of the particle angle of attack [deg]
SEGTOL	Ice	1.5	Maximum amount any segment may grow before it is divided in two [ratio of new to old segment length]
TIMSTP	Trajectory	$.999 \times 10^{-3}$	Initial value of the time step used in the integration of the particle trajectory equation
VEPS	Trajectory	.001	Accuracy criteria for the case when LXOR = 1
XORC	Trajectory	- 4.0	X-coordinate position of particle release [x_0/chord]
XSTOP	Trajectory	0.5	Maximum downstream value of x/chord for which particle trajectories are calculated
YOLIM	Trajectory	$.999 \times 10^{-4}$	Accuracy criteria for computing the surface impingement limits
YOMAX	Trajectory	.05	Initial guess for the y-coordinate of the upper surface tangent trajectory release point [y_0/chord]
YOMIN	Trajectory	-.05	Initial guess for the y-coordinate of the lower surface tangent trajectory release point [y_0/chord]
YORC	Trajectory	0.0999	Y-coordinate position of particle release [y_0/chord]

Table B-3 Interactive Inputs

Prompts	Options
Total icing time	[secs]
Time step size	[secs]
New plot options (for VAX version only)	Y/N
Plot options	0 - No plots 1 - Plot parameters 2 - Plot ice shape only
Preview beta	Y/N
Program options	1 - Use previous flow field 2 - Calculate new flow field 3 - Terminate program

B.2. Outputs

The outputs from LEWICE are the various icing parameters and the predicted ice shapes for each of the ice accretion times specified. Table B-4 is a partial listing of output parameters. These are typically in an output file, and are presented graphically after the total ice accretion computations are complete. Some of the information, such as the impingement trajectory or an ice shape, can be displayed on screen after each time step. The user has the option of displaying the data after each time step or after all time steps have been calculated.

Table B-4 Output parameters.

Parameter	Usage	Explanation
BETA	Traj and Ice	Collection efficiency
CP	Flow	Surface pressure coefficient
DICE	Ice	Thickness of the ice accreted, [m]
DT	Trajectory	Size of integration time step used for the trajectory calculation, [secs]
FFRAC	Ice	Freezing fraction

HTC	Ice	Convective heat transfer coefficient, [W/m^2°K]
I, J	All	Segment number
MDOTC	Ice	Mass flux of impinging water, [kg/s]
MDOTE	Ice	Mass flux of water vapor evaporating, [kg/s]
MDOTRI	Ice	Mass flux of surface water running in, [kg/s]
MDOTT	Ice	Total mass flux of water capable of being frozen, [kg/s]
MDOTTI	Ice	Total mass flux of water entering, [kg/s]
NSTP	Trajectory	Number of integration time steps required for trajectory calculation
PRESS	Ice	Static pressure at the outer edge of the boundary layer, [Pa]
QCOND	Ice	Conductive heat flux from the body surface, [W/m^2]
RA	Ice	Density at the outer edge of the boundary layer, [kg/m^3]
RI	Ice	Density of the ice, [kg/m^3]
S	Flow	Distance from the stagnation point to the midpoint of each segment, [m]
SEGLENGTH	Ice	Length of the body segments, [m]
TE	Ice	Static temperature at the outer edge of the boundary layer, [°K]
TSURF	Ice	Equilibrium surface temperature, [°K]
VE	Ice	Velocities at the outer edge of the boundary layer, [m/s]
VT	Flow	Non-dimensional surface velocity
X, Y	Flow	Coordinates of the midpoints of the segments describing the accreting body shape
X0, Y0	Trajectory	Coordinates of particle release location, [m]
XK	Ice	Equivalent sand-grain roughness height, [m]
XP, YP	Trajectory	Coordinates where particle either impinged upon the body or moved out of range, [m]

Appendix C: Heat Transfer Calculation

The calculation of the heat transfer coefficient involves several steps (Fig. C-1). First, the local Reynolds number, Re_l, is calculated for each segment. Re_l is then used to determine whether that segment has a laminar or turbulent boundary layer. Then, the heat transfer coefficient is calculated using either the laminar heat transfer coefficient equations or the turbulent heat transfer equations.

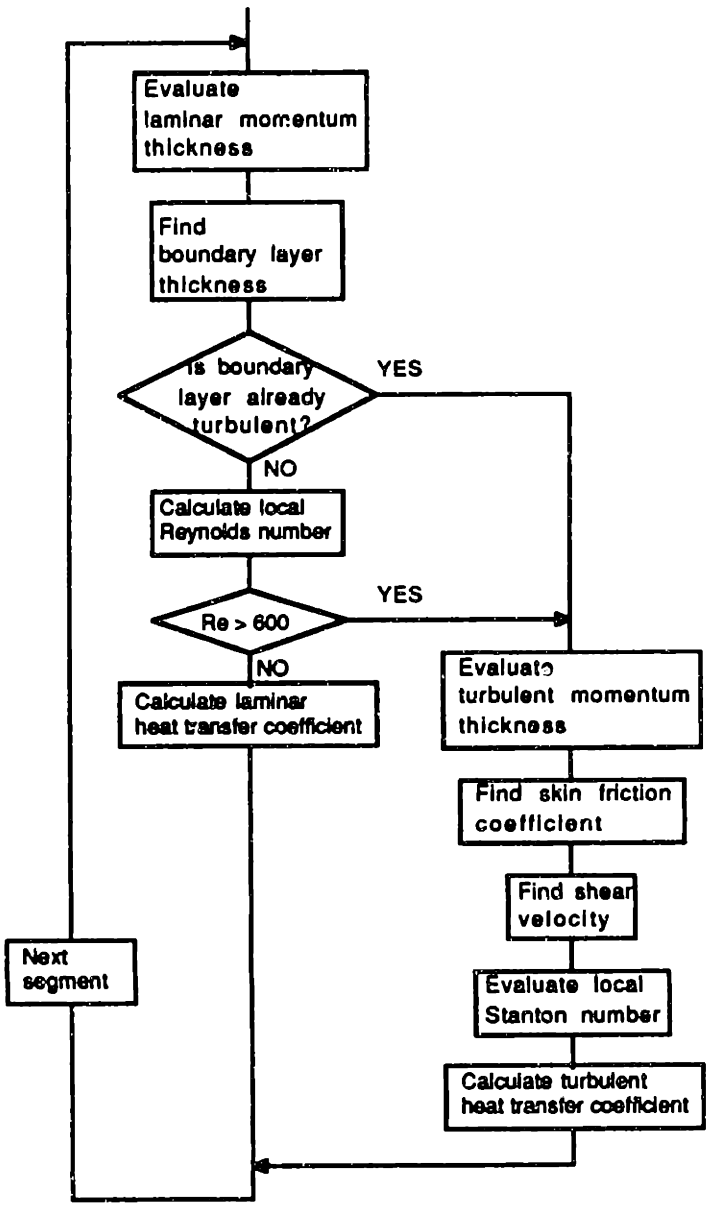

Fig. C-1 Flow chart of heat transfer calculation.

C.1. Determination of Boundary Layer Transition Location:

In order to find the local Reynolds number based on roughness element height, it is necessary to find the local velocity at distance k_s away from the surface (Fig. C-2). To find this value, the thickness of the boundary layer is determined from the momentum thickness θ_l:[14]

$$\theta_l^2 = \frac{0.45\,\nu}{u_e^6}\int_0^5 u_e^5\,ds \qquad [C\text{-}1]$$

where u_e is the surface velocity calculated by the potential flow equations. Then the boundary layer thickness, δ, is related to θ_l by:

$$\delta = 8.5\,\theta_l \qquad [C\text{-}2]$$

Then the local velocity at distance k_s from the surface, u_k, is found using the Pohlhausen approximation:[14]

$$\frac{u_k}{u_e} = \left[2\left(\frac{k_s}{\delta}\right) - 2\left(\frac{k_s}{\delta}\right)^3 + \left(\frac{k_s}{\delta}\right)^4\right] + \frac{1}{6}\frac{\delta^2}{\nu}\frac{du_e}{ds}\left(\frac{k_s}{\delta}\right)\left(1-\frac{k_s}{\delta}\right)^3 \qquad [C\text{-}3]$$

The local Reynolds number is:[12]

$$Re_l = \frac{k_s\,u_k}{\nu} \qquad [C\text{-}4]$$

When the local Reynolds number exceeds the critical Reynolds number value of 600, the boundary layer is assumed to have transitioned to turbulent.

C.2. Laminar Heat Transfer Coefficient

For the laminar boundary layer, the heat transfer, h_l, can be found by simply evaluating:[14]

$$h_l = 0.296 \frac{\lambda}{\sqrt{\nu}} \left[u_e^{-2.88} \int_0^s u_e^{1.88}\, ds \right]^{-0.5} \qquad \text{[C-5]}$$

where λ is the thermal conductivity of air.

C.3. Turbulent Heat Transfer Coefficient[20]

For the turbulent boundary layer, the process is a little more complicated. First, the turbulent momentum thickness θ_t is found from:

$$\theta_t(s) = \left[\frac{0.0156}{u_e^{4.11}} \int_{s_{tr}}^{s} u_e^{3.85}\, ds \right]^{0.8} + \theta_l(s_{tr}) \qquad \text{[C-6]}$$

where u_e is the surface velocity from potential flow calculation and $\theta_l(s_{tr})$ is the laminar momentum thickness at the laminar to turbulent transition point. Then, the skin friction coefficient, c_f, is calculated from:

$$\frac{c_f}{2} = \left[\frac{0.41}{\ln\left(\frac{864\,\theta_t}{k_s} + 2.568 \right)} \right]^2 \qquad \text{[C-7]}$$

The shear velocity, u_τ, is then evaluated using

$$u_\tau = u_e \sqrt{\frac{c_f}{2}} \qquad \text{[C-8]}$$

The roughness Stanton number, St_k, is:

$$St_k = 1.16 \left(\frac{u_\tau\, k_s}{\nu} \right)^{-0.2} \qquad \text{[C-9]}$$

The local Stanton number, St, is:

$$St = \frac{\frac{c_f}{2}}{Pr_t + \sqrt{\frac{c_f}{2}}\left(\frac{1}{St_k}\right)} \qquad [C\text{-}10]$$

where for the turbulent Prandtl number, Pr_t, value of 0.9 for air is used. Finally, the turbulent heat transfer coefficient, h_t, is calculated from the definition of the Stanton number:

$$h_t = St \cdot \rho \cdot u_e \cdot C_p \qquad [C\text{-}11]$$

where ρ is the density of air and C_p is the specific heat of air.

Appendix D Heat Transfer Coefficient Comparisons

This appendix contains the heat transfer coefficient cmparisons between the values calculated using the original LEWICE and experimental data taken by Achenbach.[15]

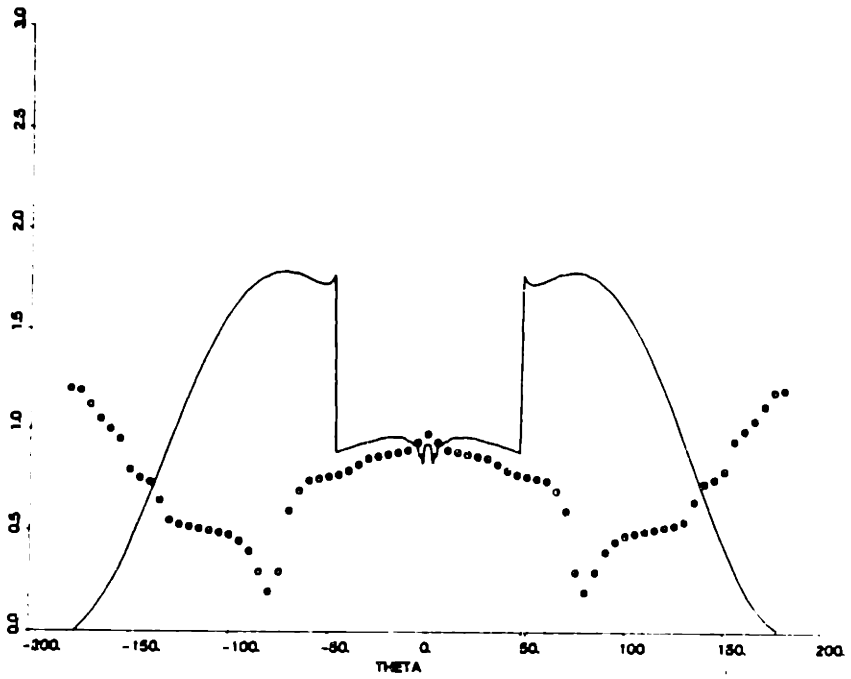

Fig. D-1 Comparison of heat transfer coefficient, Re = 4.8 x 10^4, k_s = 1.35 mm.

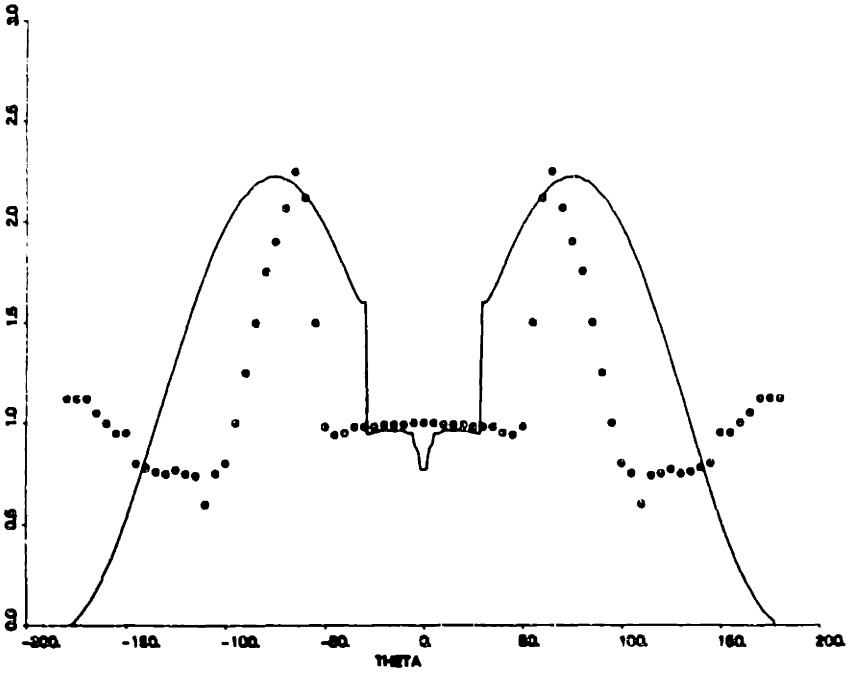

Fig. D-2 Comparison of heat transfer coefficient, Re = 7.3 x 10^4, k_s = 1.35 mm.

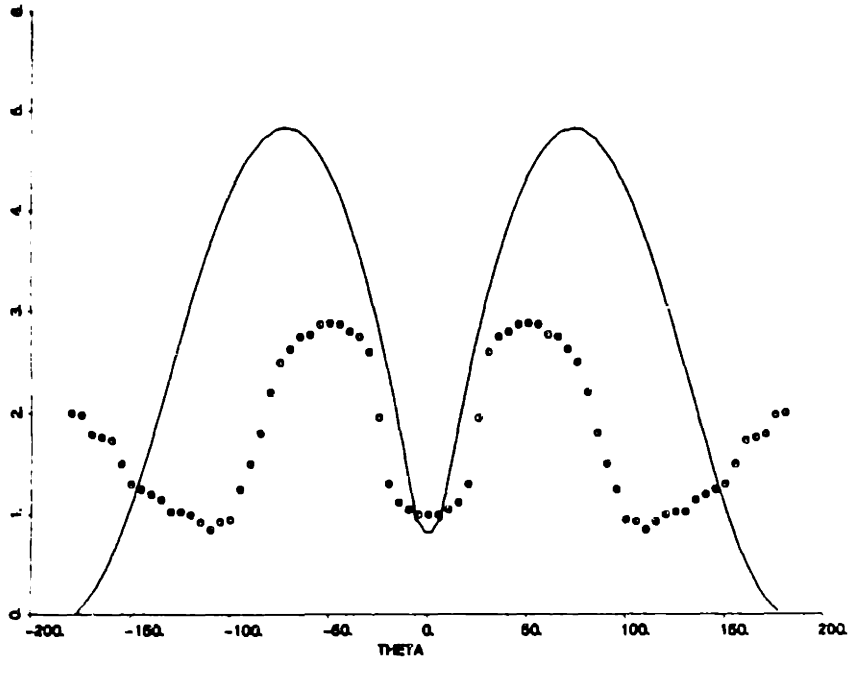

Fig. D-3 Comparison of heat transfer coefficient, Re = 2.8 x 10^5, k_s = 1.35 mm.

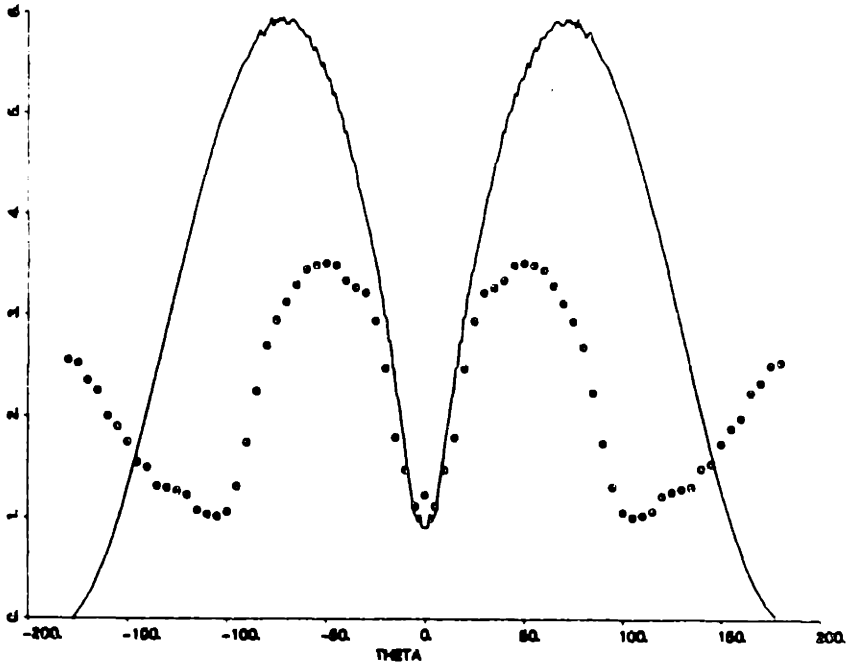

Fig. D-4 Comparison of heat transfer coefficient, Re = 3.8 x 10^5, k_s = 1.35 mm.

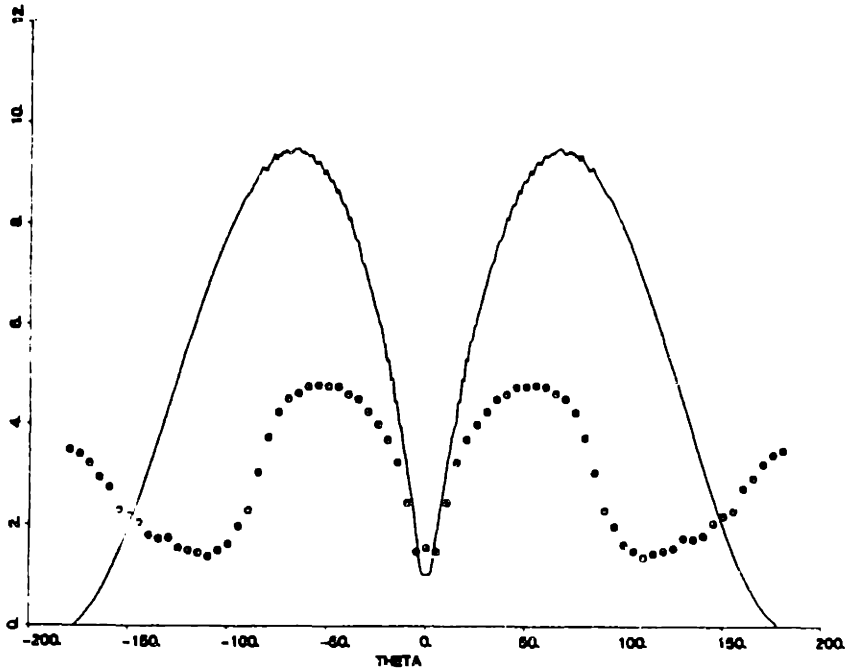

Fig. D-5 Comparison of heat transfer coefficient, Re = 8.8 x 10^5, k_s = 1.35 mm.

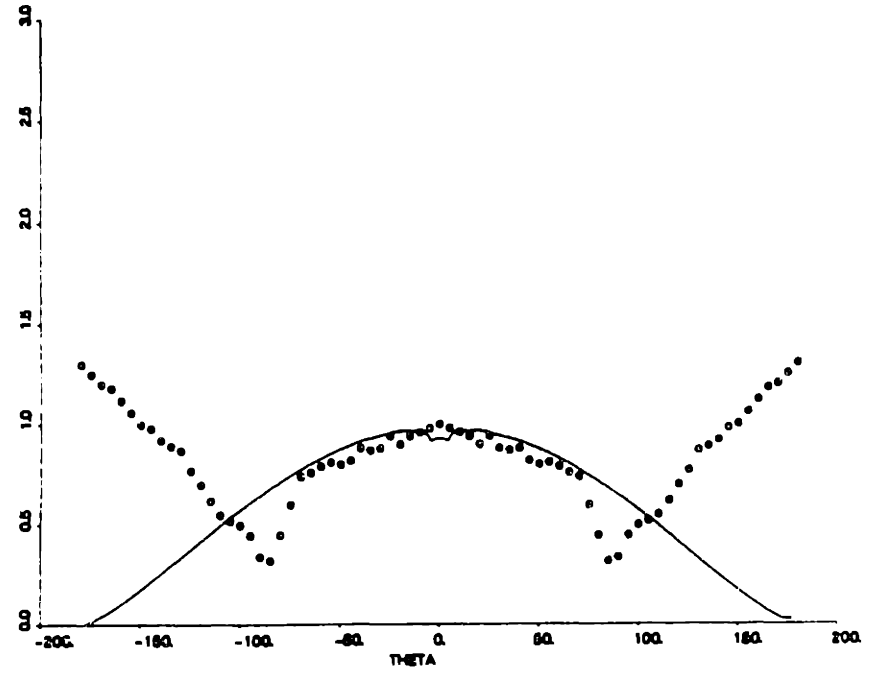

Fig. D-6 Comparison of heat transfer coefficient, Re = 7.2 x 10^4, k_s = 0.45 mm.

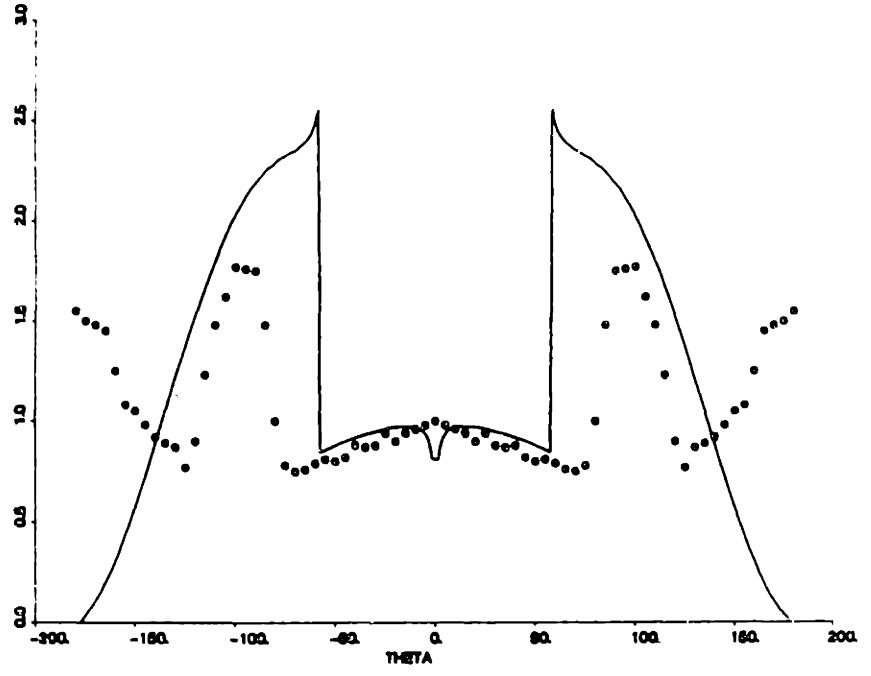

Fig. D-7 Comparison of heat transfer coefficient, Re = 1.27 x 10^5, k_s = 0.45 mm.

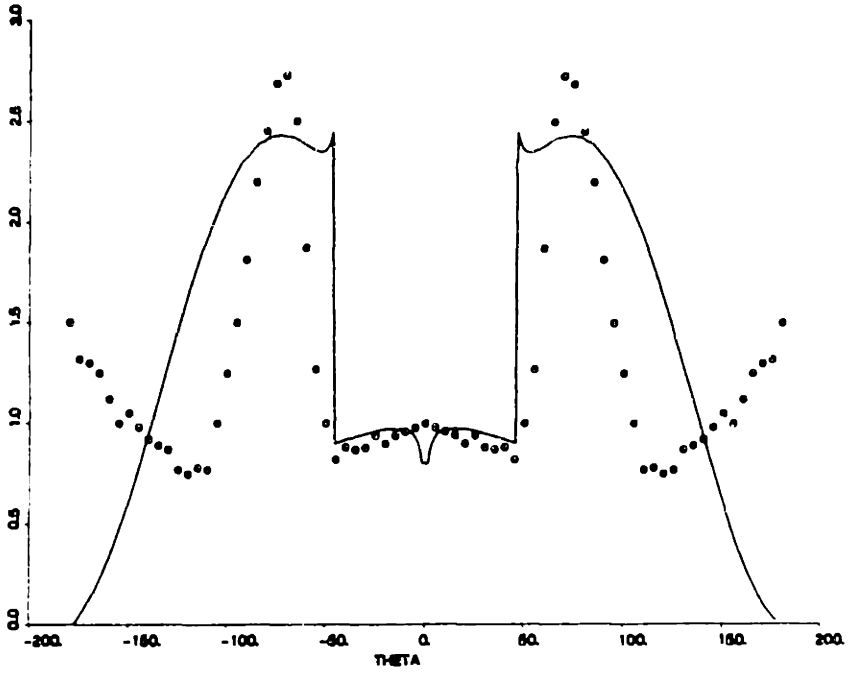

Fig. D-8 Comparison of heat transfer coefficient, Re = 1.46 x 10^5, k_s = 0.45 mm.

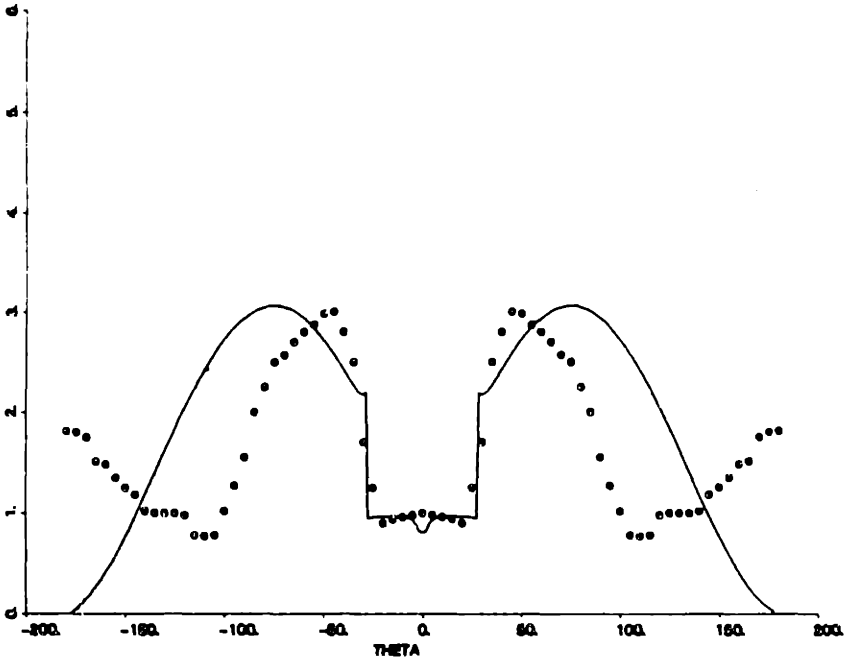

Fig. D-9 Comparison of heat transfer coefficient, Re = 2.26 x 10^5, k_s = 0.45 mm.

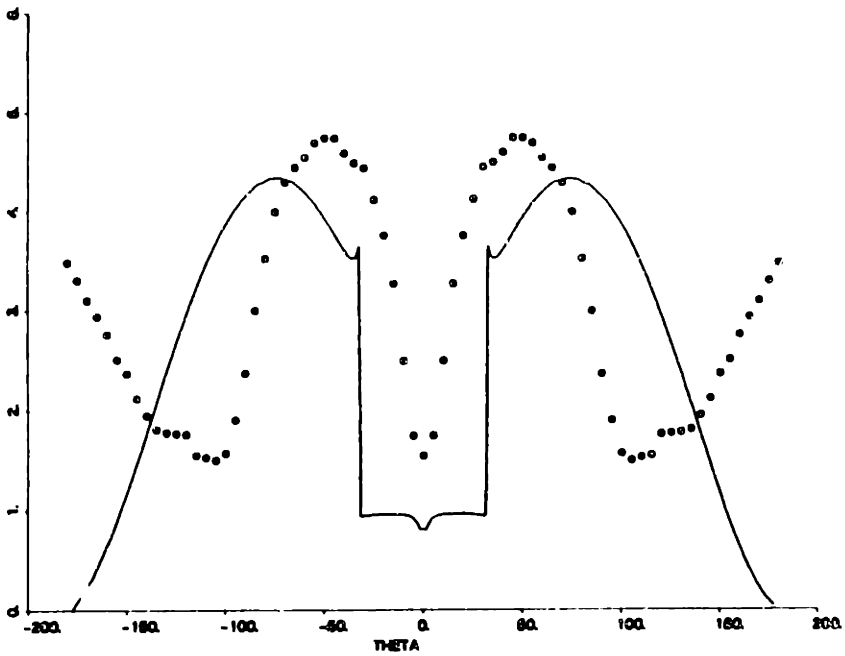

Fig. D-10 Comparison of heat transfer coefficient, Re = 8.6 x 10^5, k_s = 0.45 mm.

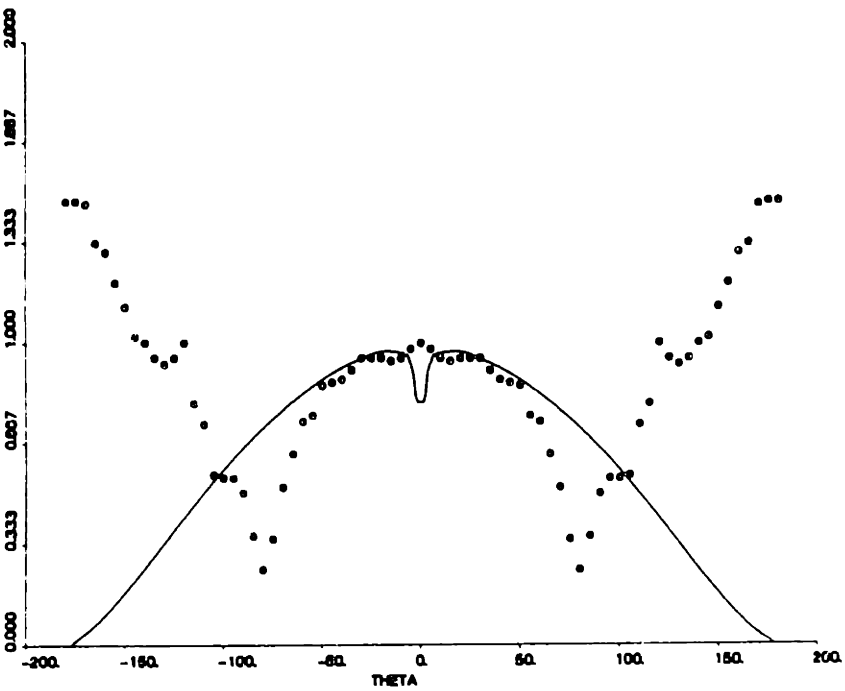

Fig. D-11 Comparison of heat transfer coefficient, Re = 9.2 x 10^4, k_s = 0.115 mm.

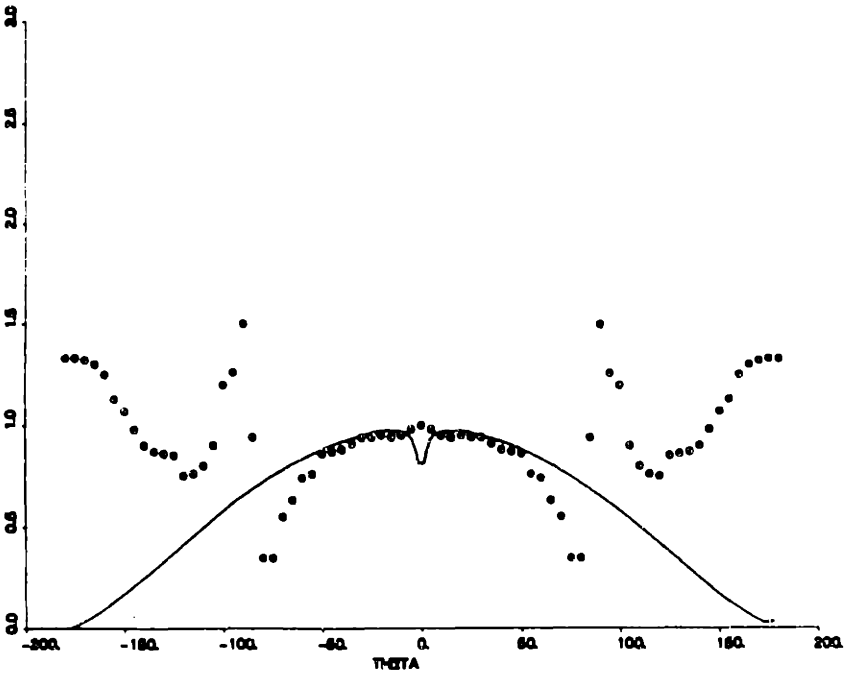

Fig. D-12 Comparison of heat transfer coefficient, Re = 1.9 x 10^5, k_s = 0.115 mm.

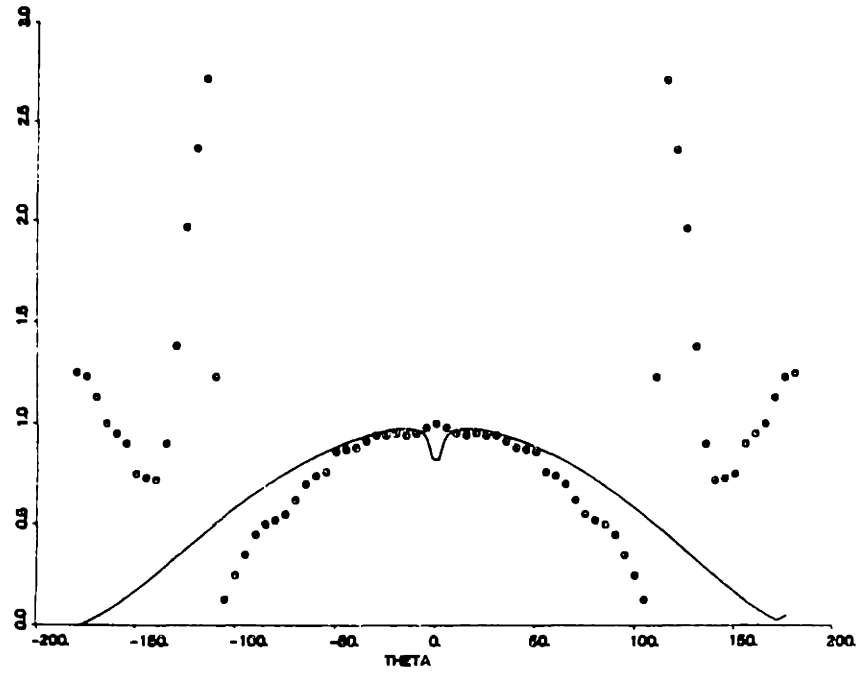

Fig. D-13 Comparison of heat transfer coefficient, Re = 4.1 x 10^5, k_s = 0.115 mm.

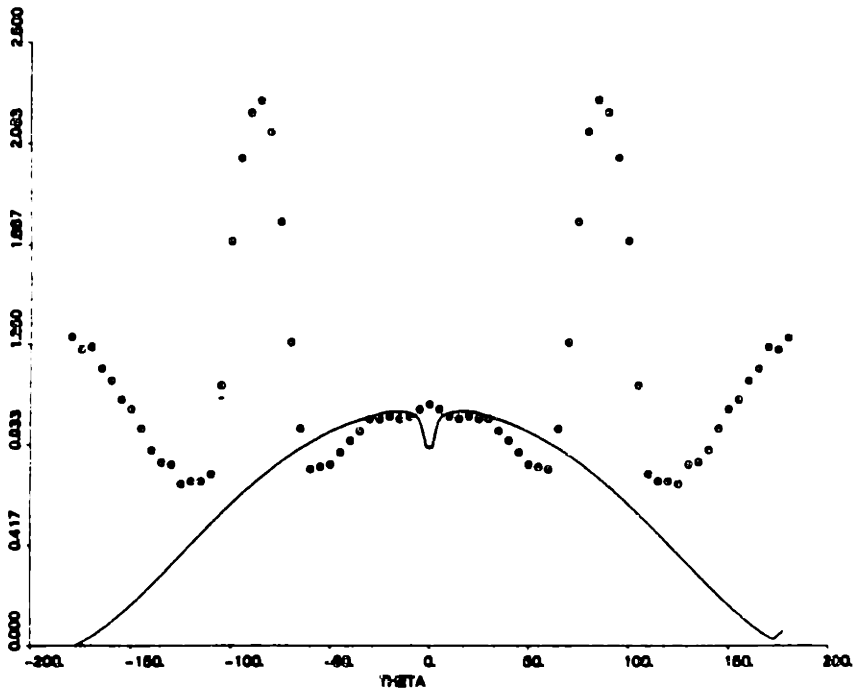

Fig. D-14 Comparison of heat transfer coefficient, Re = 5.9 x 10^5, k_s = 0.115 mm.